Radiological Characterization of TFA metallic tubes from CERN Accelerator Complex

Thesis submitted to the University of Coimbra
for the degree of Master in Engineering Physics

João Pedro SARAIVA

Geneva, September 2012

Radiological Characterization of TFA metallic tubes from CERN Accelerator Complex

Thesis submitted to the University of Coimbra
for the degree of Master in Engineering Physics

João Pedro SARAIVA

Supervisors:
Dr. João CARVALHO, UC
Dr. Robert FROESCHL, CERN

Geneva, September 2012

Abstract

The scope of this thesis consists in the radiological characterization of chilled water pipes used for air-conditioning and exposed to ionizing radiation in the PS accelerator, one of the CERN accelerators, for more than 40 years. Due to corrosion problems, the 1200 m of steel pipeline were removed from the PS tunnel during the long shutdowns between the years 2000 to 2004. The radiological characterization, that included the use of FLUKA Monte Carlo simulations and the JEREMY code, began in mid-2011 and revealed a radionuclide inventory with the presence of ^{55}Fe as dominant radionuclide and ^{60}Co as dominant γ emitter. Due to operational reasons, only 5.5% of the pipeline were characterized for validation. In the course of this work it was found that the contribution of both aforementioned radionuclides corresponds to more than 90% of the total computed IRAS factor (Indice Radiologique d'Acceptation en Stokage). Two different methods were used for the characterization of the PS pipes, yielding two different values of IRAS factor, very close to each other and both of them fulfilling the radiological ANDRA acceptance criteria. Therefore, and as expected, the PS pipes will be most probably eliminated, as soon as operationally possible, as radioactive waste towards the French TFA (Très Faiblement Actif) final repository in the Aube district.

Keywords: Ionizing Radiation, Radiological Characterization, Radionuclide Inventory, TFA Radioactive Waste

Resumo

O âmbito da presente tese assenta na caracterização radiológica de tubos de água gelada usados no arrefecimento do ar e expostos a radiação ionizante no acelerador PS, um dos aceleradores do CERN, durante mais de 40 anos. Devido a problemas de corrosão, os 1200 m de conduta de aço foram removidos do túnel do PS durante os períodos de paragem longos realizados entre os anos 2000 e 2004. A caracterização radiológica, que incluiu o uso de simulações de Monte Carlo FLUKA e o código JEREMY, foi iniciada em meados de 2011 e revelou a presença de ^{55}Fe como o radionuclídeo dominante e ^{60}Co como o emissor γ dominante. Devido a razões operacionais, apenas 5,5% da tubagem foi caracterizada para validação. No decorrer deste trabalho verificou-se que a contribuição de ambos os radionuclídeos acima mencionados corresponde a mais de 90% do valor total calculado do factor IRAS (Indice Radiologique d'Acceptation en Stokage). Dois métodos distintos foram usados na caracterização dos tubos do PS, resultando em dois valores diferentes do factor IRAS, muito próximos um do outro e ambos resultando no cumprimento dos critérios de aceitação da ANDRA. Por conseguinte, e como esperado, os tubos do PS serão muito provavelmente eliminados, tão depressa quão operacionalmente possível, como lixo radioactivo para o repositório final TFA (Très Faiblement Actif) no distrito francês de Aube.

Palavras-chave: Radiação Ionizante, Caracterização Radiológica, Inventário de Radionuclídeos, Lixo Radioactivo TFA

Table of Contents

1 Introduction **1**

2 Introductory Concepts **3**

2.1 Radioactive Decays 3

2.2 Activation and Contamination 5

2.3 Nuclear Reactions 6

2.4 Particle Spectra 9

2.5 Quantities and Units in Radiation Protection 10

3 Radioactivity at CERN **13**

3.1 CERN Accelerator Complex 13

3.2 LHC Beam Loss Profile 16

3.3 The Proton Synchrotron (PS) 17

3.4 PS Beam Loss Profile 19

3.5 The PS Chilled Water Pipes 21

3.6 Elimination Pathways of Radioactive Waste from CERN 24

3.7 ANDRA Radiological Acceptance Criteria 25

3.7.1 IRAS Factor 26

4 Strategy for Radiological Characterization **28**

4.1 Pre-conditioning 28

4.2 Radiological Characterization 29

4.2.1 Specific Activity vs. Count Rate 31

4.2.2 Dose Rate Ratio 33

5 Computer Codes for Induced Activation **38**

5.1 JEREMY 38

5.1.1 Mathematical Formulation 39

5.1.2 JEREMY Inputs 40

5.1.3 JEREMY Results 44

5.1.4 $\text{IRAS}_{\text{JEREMY}}$ 45

5.2 FLUKA 46

5.2.1 FLUKA Inputs 46

5.2.2 FLUKA Results 47

6 Analysis of the Results **51**

6.1 Spectrometry 51

6.2 Experimental Validation 53

7 Conclusions **56**

References **58**

Acknowledgements **62**

List of Figures

1.1 The PS tunnel (1958). 1

1.2 The PS pipes after the cutting process. 2

2.1 Fluence spectra for the SPS with a proton energy of 450 GeV. 10

3.1 CERN accelerator complex. 13

3.2 LHC layout. 14

3.3 ISR interim storage. 15

3.4 Loss map around the LHC ring for injection of Beam 1 (23.11.2009). . . . 17

3.5 PS proton intensity evolution over 50 years. 18

3.6 The PS complex. 18

3.7 Radiation survey around the PS ring normalized to 32 h after beam stop. 20

3.8 Septa map in the PS complex. 20

3.9 Scheme of the iced water pipes location in the PS tunnel. 21

3.10 Count rate measurement (February 2004). 22

3.11 Decay of the specific activity of the sample T37 for a cooling time of 10 years after the machine shutdown (12.11.2003). 23

3.12 Life cycle of CERN radioactive waste. 25

4.1 Location of building 573. 28

4.2 Pre-conditioning process. 30

4.3 Radiological characterization process. 31

4.4 Normalization methods. 32

4.5 γ-spectrometer (Ge detector), in situ γ-spectrometer (Ge detector) and 4π gamma counter. 32
4.6 Specific activity (RADOS RTM661/440) vs. count rate (FHZ 512 BGO). . 33
4.7 Geometry approximation of the compacted pipe pieces. 34
4.8 Distance between emission and measurement points. 35

5.1 JEREMY code dataflow. 39
5.2 Neutron fluence spectra with a proton beam momentum of 14 GeV c^{-1}. 41
5.3 Optical Emission Spectroscopy analyser (PMI-Master pro). 42
5.4 Equivalent dose rate (top view). 48
5.5 Equivalent dose rate (lateral view). 48
5.6 Equivalent dose rate for a layer of 0.5 cm directly above the pipe piece. . 49
5.7 Simulation and analytical computation of the equivalent dose rate. . . . 49

6.1 Activity build-up and decay of ^{60}Co and ^{55}Fe over time. 53
6.2 Histogram of the net count rate dispersion. 54

List of Tables

2.1 Radioactive decay processes. 4

2.2 Nuclear reactions. 8

2.3 Pi and eta mesons data. 9

2.4 Protection quantities. 12

3.1 Gamma spectrometry results from pipes T16 and T37. 23

3.2 CERN's exemption limits for radionuclides of artificial origin. 24

3.3 ANDRA's technical terms. 26

3.4 TFA class, reporting threshold and LDF of some radionuclides. 27

5.1 Chemical composition of the PS pipes (PMI-Master pro). 42

5.2 Chemical composition analysis of a stainless steel sample. 43

5.3 Specific activities by unit loss rate of dominant radionuclides. 44

5.4 Total specific activities by unit loss rate. 45

6.1 ^{60}Co and ^{55}Fe specific activities and ratio between both values. 52

6.2 ^{60}Co and ^{44}Ti specific activities and ratio between both values. 53

6.3 $IRAS_{colis}$ of both methods of normalization. 55

List of Acronyms

ALARA	As Low As Reasonably Achievable
ANDRA	Agence Nationale pour la Gestion des Déchets Radioactifs
BGO	Bismuth Germanium Oxide
CERN	European Organization for Nuclear Research
CSTFA	Centre de Stockage des déchets Très Faiblement Actifs
CT	Continuous Transfer
DR	Dose Rate
EIG	Ecole d'Ingénieurs de Genève
FA	Faiblement Actif
FLUKA	FLUktuierende KAskade
HA	Hautement Actif
HEPIA	Haute École du paysage, d'Ingénierie et d'Architecture
HSE	Occupational Health & Safety and Environmental Protection Unit
ICRP	International Commission on Radiological Protection
ICRU	International Commission on Radiation Units & Measurements
INC	IntraNuclear Cascade Model
IP	Interaction Point
IR	Insertion Region
IRAS	Indice Radiologique d'Acceptation en Stokage
ISR	Intersecting Storage Rings
LDF	Limite de Déclaration Forfaitaire
LHC	Large Hadron Collider
LSC	Liquid Scintillation Counting
MA	Moyennement Actif
MDA	Minimum Detectable Activity
MTE	Multi-Turn Extraction

MU	Magnet Unit
OES	Optical Emission Spectroscopy
PMT	Photomultiplier Tube
PS	Proton Synchrotron
PSB	Proton Synchrotron Booster
RF	Radiofrequency
RP	Radiation Protection Group
RPP	Rectangular Parallelepiped
SPS	Super Proton Synchrotron
SS	Straight Section
TFA	Très Faiblement Actif
XRF	X-Ray Fluorescence Spectrometry
ZDN	Zone à Déchets Nucleaire

CHAPTER 1

Introduction

The work described in this document emerged from the need to perform the radiological characterization of 1200 m of a chilled water pipeline, exposed during several years to ionizing radiation on the top of the Proton Synchrotron (PS) tunnel (see Fig. 1.1). The pipeline was used, for more than 40 years, for air-conditioning of the PS tunnel, being subsequently removed due to problems of corrosion. The beam losses occurring along the PS accelerator resulted in the activation of the pipeline, implying that it had to be treated as radioactive waste and eliminated according to its level of induced radioactivity.

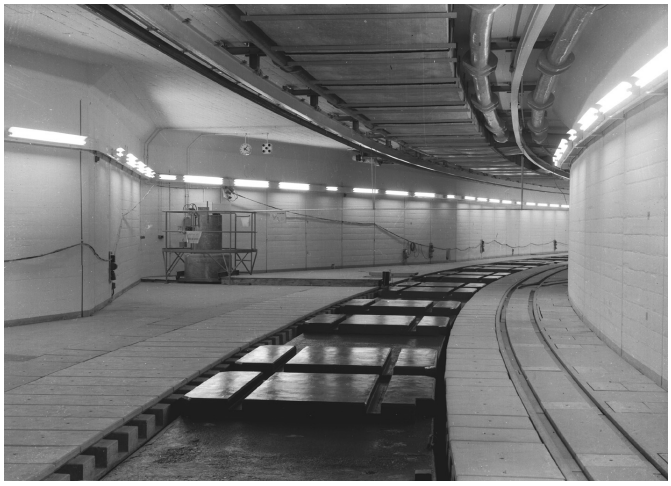

Figure 1.1: The PS tunnel (1958).

The permanent storage at the CERN site of radioactive waste produced in its own installations is neither practicable nor permitted by the authorities of both CERN Host States. Moreover, the expected growing rate of activated waste due to the higher energies and intensities achieved with the Large Hadron Collider (LHC), increases the need of eliminating all these materials to a final repository.

The outline of the thesis is as follows. Chapter 2 presents the physics and technical terms used throughout this document, such as the most common radioactive decay modes and nuclear reactions, as well as the different quantities and units used in radiation protection and relevant for this work.

Chapter 3 presents a short description of the CERN accelerator complex, including the LHC and PS layouts, the beam loss profile and the consequences of those losses in the surroundings of both accelerators. The historical data of the PS chilled water pipes (see Fig. 1.2), the different elimination pathways of the radioactive waste produced at CERN and the ANDRA[1] radiologial acceptance criteria are also outlined in this chapter.

Figure 1.2: The PS pipes after the cutting process.

Chapter 4 describes the pre-conditioning process and two different methods used for the radiological characterization of the PS pipes. Thereafter, the computer codes used in the course of the characterization as well as the inputs and results of both codes are discussed in chapter 5.

Finally, chapter 6 presents the results of the measurements performed for validation of both processes of radiological characterization of the PS pipes, while chapter 7 summarizes the results achieved with the present work.

[1]Agence Nationale pour la Gestion des Déchets Radioactifs (French national agency for radioactive waste management).

CHAPTER 2

Introductory Concepts

2.1 Radioactive Decays

Exposure to radioactivity is a constant concern for those who work in radiation protection. Radioactivity can be defined as a spontaneous nuclear disintegration, generally accompanied by the emission of ionizing radiation. Radioactivity occurs as the result of nuclear instability, and in order to get closer to stability, the unstable nuclei (or radionuclides) rearrange themselves emitting some type of radiation, where the most important are the well known alpha, beta and gamma radiation.

Tab. 2.1 shows a non-exhaustive list of decay modes, leaving out decays infrequent or not relevant for the present work, as spontaneous fission and proton emission.

The emitted radiation[1] during a radioactive decay is said to be ionizing if it can ionize matter, ejecting electrons from atoms of surrounding matter. Secondary ionizations can occur if enough energy is transferred to ejected electrons, in which case these high-energy electrons are called δ-rays [4]. The energy threshold required to produce ionizations is about 10 eV, the order of magnitude of first ionization potentials of typical materials[2].

About 3000 nuclides have already been experimentally observed. Of these, less than 10% are stable [5] while the remaining are radionuclides, i.e. sooner or later they undergo a radioactive decay. The rate at which each of these decays occur can be stated

[1] Includes electromagnetic and corpuscular radiation.

[2] Examples of first ionization potentials: carbon: 11.26 eV, hydrogen: 13.60 eV, oxygen: 13.62 eV, iron: 7.90 eV. In the case of electromagnetic radiation, photons with an energy of 10 eV are in the ultraviolet region: 3.1 eV to 124 eV (wavelength of 400 nm to 10 nm).

Decay Mode	Description	Reaction	Example
Alpha Decay (α)	Emission of an alpha particle (^{4}He). The alpha decay is the most efficient way for heavier nuclei to reduce both mass and charge.	${}^{A}_{Z}P \rightarrow {}^{A-4}_{Z-2}D + {}^{4}_{2}He$	${}^{238}_{92}U \rightarrow {}^{234}_{90}Th + \alpha$
Beta-minus Decay (β^-)	High energy electron (β^-) and anti-neutrino ($\overline{\nu}$) emission from a nucleus with excess number of neutrons (nuclide below the line of stability in the Chart of Nuclides).	$n \rightarrow p + \beta^- + \overline{\nu}$	${}^{60}_{27}Co \rightarrow {}^{60}_{28}Ni + \beta^- + \overline{\nu}$
Beta-plus Decay (β^+)	Positron (β^+) and neutrino (ν) emission from a nucleus with an excess of protons (i.e. above the line of stability in the Chart of Nuclides). Two 0.511 MeV annihilation photons, emitted in opposite directions to conserve momentum, accompanies always the positron annihilation.	$p \rightarrow n + \beta^+ + \nu$	${}^{22}_{11}Na \rightarrow {}^{22}_{10}Ne + \beta^+ + \nu$
Electron Capture (EC)	Capture of an electron from the inner K or L shells* in order to reduce the number of protons. When the beta-plus decay is energetically possible, as happens† with ^{22}Na but not with ^{55}Fe, both processes are competing mechanism. The vacancies left from the capture events are filled by electrons from outer shells resulting in X-rays and Auger electrons‡ emission.	$p + e^- \rightarrow n + \nu$	${}^{55}_{26}Fe + e^- \rightarrow {}^{55}_{25}Mn + \nu$
Isomeric Transition (IT)	After a radioactive decay, the transforming nucleus is frequently in an excited state. Most of them are short-lived excited states ($< 10^{-9}\,s$) and returns to the ground state through gamma emission $\left({}^{A}_{Z}P^* \rightarrow {}^{A}_{Z}P + \gamma\right)$. For long-lived states (metastable (or isomeric) states: lifetime $> 10^{-9}\,s$) the gamma emission is thought as a separate event and known as an isomeric transition (IT).	${}^{Am}_{Z}P \rightarrow {}^{A}_{Z}P + \gamma$	${}^{137m}_{56}Ba \rightarrow {}^{137}_{56}Ba + \gamma$
Internal Conversion	Ejection of an orbital electron by a short or long-lived excited nucleus. The excitation energy is directly transferred to an inner shell electron, ejecting it from the atom. Therefore, Internal conversion and gamma emission compete§ to relieve excitation energy held by transformed nuclei. To fill the electron shell vacancy, the internal conversion is followed by X-rays and Auger electrons emission.	${}^{A}_{Z}P^* \rightarrow {}^{A}_{Z}P^+ + e^-$	${}^{137m}_{56}Ba \rightarrow {}^{137}_{56}Ba^+ + e^-$

* Most capture events involve electrons from K-shell (of the order of 90%), but also from L-shell ($\sim$10%) and, with a much lower probability, from M-shell ($\sim$1%). [1]

† ^{22}Na branching ratio: $\sim$90.5% of the transitions occur through β^+ while $\sim$9.5% through EC. [1]

‡ The Auger effect can be seen as an "inner photoelectric effect" [1]: the X-ray produced with the filling of a inner vacancy can interact with an outer shell electron, ejecting it from the atom (Auger electron).

§ ^{137m}Ba branching ratio: $\sim$89.9% of the energy is released through isomeric transition with a $\gamma = 661.7$ keV while $\sim$11.1% occurs by internal conversion. [2]

Table 2.1: Radioactive decay processes. [1, 3]

in terms of the decay constant[3] (λ), mean lifetime[4] (τ) or half-life[5] ($t_{1/2}$). These quantities are related as shown in Eq. 2.1.1

$$\lambda = \frac{1}{\tau} = \frac{ln2}{t_{1/2}}. \tag{2.1.1}$$

The well known radioactive decay law

$$N(t) = N_0\, e^{-\lambda t}, \tag{2.1.2}$$

with *N(t)* being the number of radionuclei present at time t in a radioactive material and N_0 the initial number (at t = 0 s), can be rewritten multiplying both sides of the expression by the decay constant, resulting in the activity of the radioactive sample (see Eq. 2.1.3 and 2.1.4), i.e. the mean number of nuclear transformations that occur in the sample per unit time (decay rate).

$$\lambda N(t) = \lambda N_0\, e^{-\lambda t} = -\frac{dN(t)}{dt}, \tag{2.1.3}$$

$$A(t) = A_0\, e^{-\lambda t}, \tag{2.1.4}$$

where $A(t) = -dN(t)/dt$ and $A_0 = \lambda N_0$.

The SI derived unit of activity A is the becquerel (Bq), where 1 becquerel corresponds to 1 decay or impulse per second (1 Bq = 1 s^{-1} = 1 dps = 1 ips). The activity of a radioactive sample can be normalized, for example by dividing it through the mass M of the sample (see Eq. 2.1.5), yielding the specific activity a often expressed, also throughout this document, in Bq g^{-1}.

$$a = \frac{A}{M} \tag{2.1.5}$$

2.2 Activation and Contamination

There are two categories of processes whereby nuclei can emit radiation of some form: radioactivity, already described in previous section, and nuclear reactions that

[3]The decay constant can be defined as the radionuclide decay probability per unit time for an infinitesimal time interval. Then, a stable nuclide have $\lambda = 0$. [5]

[4]Time at which the initial population of radionuclides is reduced to 1/e of its initial value.

[5]Time for half of the radionuclei to undergo radioactive decay.

can occur, for example at CERN, when particles collide with matter and cause emission of radiation and production of radioactive materials. This bombardment or irradiation of matter by particles, making it radioactive, is called activation.

It's important to distinguish activation from contamination. Both generate radioactive materials but through processes completely different. Radioactive contamination occurs when a radioactive substance is deposited on a nonradioactive surface. Sometimes the surface contamination can easily be removed (non-fixed contamination), for example, by washing it. With activated materials this cannot be done given that usually the whole material was exposed to irradiation and therefore the radioactive nuclei are dispersed over the whole material.

2.3 Nuclear Reactions

Two general effects characterize the passage of particles through matter: energy loss and trajectory deflection. For charged particles these effects are primarily due to electromagnetic interactions, mainly inelastic scattering with orbital electrons [4]. Reactions with nuclei involving the strong interaction are rarer as consequence of the short range of this force: 10^{-15} m, the typical size of nuclei [6]. Moreover, nuclei are typically 100 000 times smaller than the distance between them in solid matter [7]. The combination of both effects explain why neutrons are very penetrating particles, since their primary[6] interaction is through the strong nuclear force with nuclei.

When a particle strikes a nucleus, two classes of collisions can happen: elastic[7] and inelastic[8] scattering. Independently of energy and type of incident particles, elastic scattering from nuclei is always present [8]. The incident particle transfers part of its energy to the recoil nucleus but the event do not contribute to activation since no new particles are created. For its part, inelastic scattering contribute to induced activity only if unstable particles are created.

During a nuclear reaction, an external particle comes in such close contact to the atomic nucleus that they interact, most of the time via the very short-range strong

[6]Neutrons are also subject to the electromagnetic and weak forces [4]. In materials with unpaired electrons, neutrons may interact through a dipole-dipole interaction between the magnetic moments of the neutron and the unpaired electron [7].

[7]During elastic collisions the identity of particles do not change and the total kinetic energy is conserved.

[8]In opposition to elastic scattering, during an inelastic collision with a nucleus, part of the kinetic energy of the interacting particles is dissipated through the nucleus excitation and/or with production of new particles.

force. As leptons[9] are not subject to this interaction, they rarely interact with nuclei [9]. Hadrons[10], in turn, have the ability to interact with nuclei but for that to happen, positively charged hadrons, such as protons, must overcome the Coulomb potential barrier of the nucleus. For example, the nuclear reaction ^{56}Fe(p,n)^{56}Co only occurs for protons with energies higher than about 5 MeV, while the reaction ^{56}Fe(n,γ)^{57}Fe is independent of the neutron energy since the neutron is not repelled by the electrostatic Coulomb force exerted by the nucleus [8].

The most common nuclear reactions are listed in ascending order of energies and described on Tab. 2.2.

Hadronic showers occur when incoming primary hadrons have energies higher than few tens of MeV. In such case, secondary particles have enough energy to collide with downstream nuclei and produce more particles, until the initial energy is converted to many particles of low energy that eventually deposit that energy within the medium by atom ionizations and excitations [15, 16].

By increasing the energy of primaries upwards 290 MeV[11], the production of pi mesons[12] starts to be significant. The π^0 meson and at higher energies the eta (η) meson decay into two photons by electromagnetic annihilation (see Tab. 2.3). At this energy level ($>> 2m_e c^2$), pair production is the dominant photon interaction with matter. The very energetic e^- and e^+ created by pair production, in turn, lose most of their energy emitting energetic bremsstrahlung[13] photons. Hence, the combined effect of pair production and bremsstrahlung emission at high energies gives rise to an electromagnetic shower. Part of the energy of the hadron shower is, therefore, transferred to produce a cascade of photons, electrons and positrons that eventually deposit their remaining energies by ionizing the atoms of the material [4, 15, 16, 19].

The photons created during a electromagnetic shower can also interact with nuclei. Absorbing a photon, the nucleus goes to an excited state and release this excess of energy as in previous interactions, emitting one or more nucleons. These nuclear

[9] Lepton are fundamental particle not subject to the strong interaction [6].

[10] The strong interaction only acts between quarks. Hadrons are composite particles made of quarks (q). There are three subgroups of hadrons: baryons (qqq), antibaryons ($\overline{q}\overline{q}\overline{q}$) and mesons ($q\overline{q}$). [6]

[11] Threshold energy for pion production by nucleon - nucleon interaction with free nucleons (the threshold energy for nucleons in nuclei is lower due to the Fermi motion). [15, 17, 18]

[12] The pi mesons or pions (π^+, π^- and π^0) are the lightest and most common of the mesons. Due to the conservation of electrical charge and flavour, the π^+ and π^- can decay only through the weak force, while the π^0 decays electromagnetically through quark-antiquark annihilation. [6]

[13] The emission of bremsstrahlung photons occurs when a charged particle (generally electrons and positrons since the emission probability varies with the inverse square of the particle mass) suffer an acceleration due to the electric field of another charged particle (primarily by atomic nuclei). [4]

Thermal* and slow neutron reactions ($< \sim$10 MeV)	
Elastic scattering X(n, n)X	Principal mechanism of energy loss for neutrons up to 1 MeV. The internal energy of the nucleus is unaffected meaning that no energy is transferred into nuclear excitation. The linear momentum and kinetic energy of the system are conserved, however, the neutron usually transfers part of its energy to the recoil nucleus.
Inelastic scattering X(n, n')X* (without nature change of interacting particles)	Neutron absorption by a nucleus forming a compound nucleus that subsequently emits a secondary neutron of lower kinetic energy. The original nucleus, left in an excited state, decays afterwards by γ-ray emission. The neutron energy must be higher than about 1 MeV in order to excite the nucleus.
Radiative neutron capture ${}^{A}_{Z}X(n,\gamma){}^{A+1}_{Z}X$	Absorption of a neutron by a nucleus that, after some time, decays to its ground state by γ emission. The radiative capture is most likely to occurs with thermal and slow neutrons since, usually, the cross-section† for neutron capture varies approximately with $\sim 1/v$ where v is the neutron velocity [4].
Particle ejection X(n, x)Y x = p, α	After absorbing a neutron, the energy excitation level of the compound nucleus is high enough to cause it to eject a proton or α-particle. The remaining nucleus can still be in an excited state and decays through γ emission. The particle ejection starts to be observed with thermal and slow neutrons for light target nucleus, whereas for heavier elements, higher energies of the incoming neutrons are required.
Fission (n, f)	Most likely to occur at thermal energies, an heavy target nucleus absorbs a neutron and splits into two similarly sizes fragments (f) plus some neutrons.
Medium energy reactions (few MeV up to $\sim$50 MeV)	
Particle ejection (evaporation) X(i, j)Y i = p, n j = n, p, 2n, d, α,...	The energy is high enough for a incoming proton to be absorbed by the target nucleus and form a excited compound nucleus. After some time, the energy is released by ejecting sequentially one or more nucleons or even heavier particles, each with relatively low kinetic energy (process known as "evaporation"). This process leaves generally the residual nucleus in an excited state that dissipates the energy by γ emission. Similar reactions occurs also with neutrons.
High energy reactions (> several tens of MeV)	
Spallation of high energy hadrons $X(i,\ x_1 n + x_2 p + ...)Y$ $i = p, n, \pi^+, \pi^-, ...$ $x_{1,2...} \in \mathbb{N}_0$	An excited nucleus, knocked by a hadron with relatively high energy (tens or hundreds of MeV), decays by evaporation of several particles (n, p, π, d, α,...). Due to the energy involved, a large number of light particles are emitted, leading to a target residue considerably lighter than the original nucleus and generally unstable. Some of the struck nucleons by the primary may be directly ejected from the nucleus with relatively large kinetic energy. The others make secondary collisions with nucleons of the same nucleus before escaping or being caught by it (IntraNuclear Cascade model (INC)) [10]. The secondaries ejected during the spallation reaction may have enough energy to induce further reactions, giving rise to a hadron shower. The foremost characteristic of spallation reactions is the emission of many light fragments, mostly neutrons [11]. Typically, a lead target hit by a 1 GeV proton yields about 25 neutrons [12]. Another channel for de-excitation of the residual nucleus is through high energy fission that can take place as alternative to spallation.

* $K = K_B T$ @20°C $\simeq$ 0.025 eV ($2K = mv^2 \Leftrightarrow v \simeq 2190$ m s^{-1}).

† For incident particles of a fixed energy, each interaction mechanism has a constant probability per unit path length to occurs. This probability is usually expressed in terms of the cross section (σ) per nucleus:

σ (cm^2) = reaction rate per nucleus (s^{-1}) / flux of incident particles (cm^{-2} s^{-1}).

The barn is the traditional unit of cross section (1 barn (b) = 10^{-24} cm^2). [13]

Table 2.2: Nuclear reactions. [8, 14]

Particle	Content	Rest mass [MeV c^{-2}]	Lifetime [s]	Principal decay modes
Pion plus (π^+)	$u\bar{d}$	140	2.6×10^{-08}	$\mu^+ + \nu_\mu$
Pion minus (π^-)	$d\bar{u}$	140	2.6×10^{-08}	$\mu^- + \bar{\nu}_\mu$
Pion zero (π^0)	$(u\bar{u} - d\bar{d})/\sqrt{2}$	135	8.5×10^{-17}	$\gamma + \gamma$
Eta (η)	$(u\bar{u} + d\bar{d} - 2s\bar{s})/\sqrt{6}$	547	1×10^{-18}	$\gamma + \gamma$

Table 2.3: Pi and eta mesons data. [20, 21]

interactions induced by γ-rays are known as photonuclear or photodisintegration reactions: (γ, n), (γ, 2n), (γ, p), (γ, α), etc. Photonuclear reactions also include resonance mechanisms, out of scope of this work.

Secondaries produced during a photonuclear reaction can in turn interact with other nuclei contributing also to the overall activity of the material. On the other hand, the electrons (and positrons) of the shower contribute indirectly to the material activation through the creation of high energy photons. The threshold for photonuclear reactions is around 10 MeV (or higher for most nuclei except for ^{2}H and ^{9}Be which have a threshold of the order of 2 MeV), nevertheless its probability of occurrence is much smaller than that for others photon interaction mechanisms at this energy level. [8, 22].

2.4 Particle Spectra

It was seen that the activation produced by a high energy hadron striking a nucleus arises from the residual nucleus, likely converted to a radionuclide, and from the reaction products of energetic secondaries that participated in further spallation reactions creating unstable nuclei. Therefore, the activation induced in high energy particle accelerators will depend on several factors, namely: the primary beam loss (beam loss rate, energy and particle type), the spectra of the secondaries produced by the beam loss (particle spectra), the composition and size of the exposed material and the production cross sections of the possible radioisotopes. Furthermore, the amount of radionuclides present at a given time and in a given material will also depend on their half-life as well as on the activity build-up and decay, i.e. on the time that the accelerator was in operation (irradiation time) and the time since operation stopped (cooling time). [9]

The activating particles present in the radiation environment, i.e. the particle spectra of the radiation field, are of particular relevance for the calculation of the radioactiv-

ity induced in materials and equipments close to the accelerator. These spectra of secondaries can be obtained by Monte Carlo simulation, as the FLUktuierende KAskade (FLUKA) code. An example of fluence spectra for p, n, π^+ and π^- per primary beam particle, obtained by FLUKA simulation, for the Super Proton Synchrotron (SPS) with a primary beam loss of one proton per second of 450 GeV, can be seen in Fig. 2.1. [23, 24]

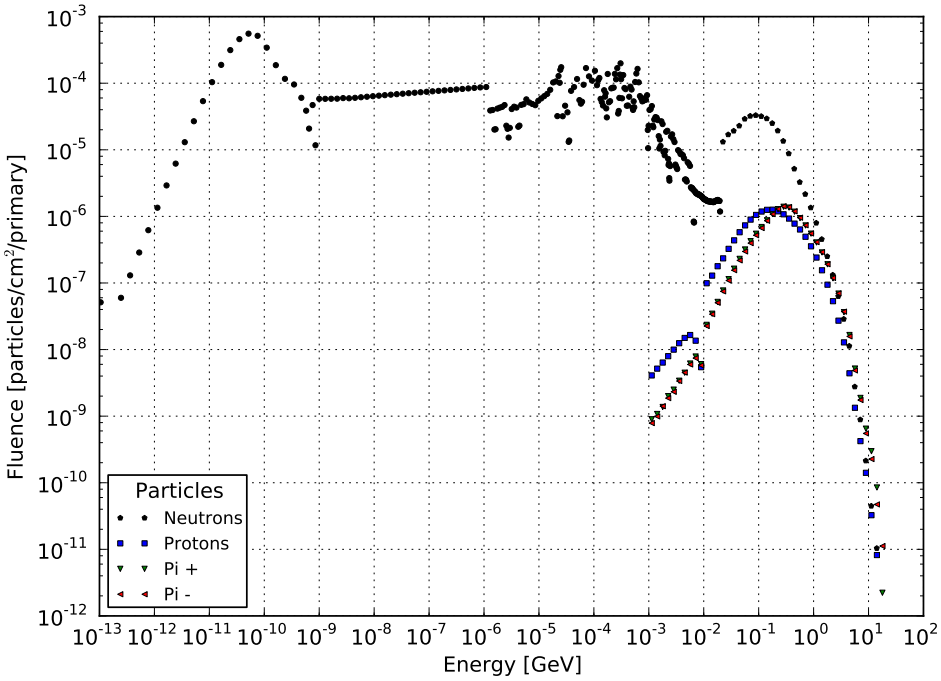

Figure 2.1: Fluence spectra for the SPS with a proton energy of 450 GeV. [24]

2.5 Quantities and Units in Radiation Protection

Since the list of radiation quantities and units is extensive, only those relevant for this work are referred to below. Three physical quantities used in radiation protection must be mentioned: the activity A, already described, the fluence Φ and the absorbed dose D. It was seen that the activity corresponds to the mean number of nuclear decays occurring in a given material per unit time and that its SI derived unit is the becquerel. An older unit sometimes used for measuring the activity is the curie (Ci), where 1 Bq = 27 pCi [20].

The fluence Φ is defined by the International Commission on Radiation Units and Measurements (ICRU), for the common situation where interactions due to the radiation field are independent of the direction of the incoming particles, as

$$\Phi = \frac{dN}{da}, \tag{2.5.1}$$

where dN is the number of particles incident on a sphere of cross-sectional area da. The sphere of differential cross-sectional area is used to express the idea that da is perpendicular to the direction of each particle. The SI derived unit of fluence is m^{-2}. The fluence can also be seen as the time integral of the incident flux of particles through da over the exposure duration. [13, 25, 26]

Materials with different physical and chemical properties, subjected to the same radiation exposure, will in general absorb different amounts of energy, i.e. they will have different absorbed doses D. The absorbed dose is defined as the mean energy deposited by ionizing radiation per unit mass of the absorber, and it can be written as

$$D = \frac{d\bar{\varepsilon}}{dm}, \tag{2.5.2}$$

where $d\bar{\varepsilon}$ is the mean energy imparted by ionizing radiation to a mass element dm of the absorber. The SI derived unit of absorbed dose is the gray (Gy), where 1 Gy = 1 J kg^{-1}. Another unit, less used, is the rad (radiation absorbed dose), with 1 Gy = 100 rad. [13, 25]

Besides the physical quantities, two different groups of dose related quantities were established by the ICRU and ICRP for radiation protection applications: the protection quantities that take into account the human body properties and the operational quantities for exposure monitoring [26–28]. The protection quantities, described on Tab. 2.4, are used for quantification of the extent of the human body exposure to ionizing radiation from both internal (intakes of radionuclides) and external irradiation [20].

The protection quantities are not measurable in practice and for that reason they are not directly used as quantities for calibration of radiation monitors. Therefore, operational quantities are used for the assessment of effective dose or equivalent dose in tissues or organs. The operational quantities are measurable quantities that adequately represent the protection quantities related to radiation exposures, providing a conservative estimate or upper limit for the value of these protection quantities. [20, 26, 27]

For monitoring external exposures of radiation, operational dose equivalent quantities were defined: the ambient dose equivalent H*(10) and the directional dose equivalent H′(0.07) for area (or ambient) monitoring, and the personal deep dose equivalent $H_p(10)$ and the personal surface dose equivalent $H_p(0.07)$ for individual monitoring, all expressed in sieverts. Radiation protection monitoring instruments as dosimeters and

Protection Quantity	Definition	Unit
Organ absorbed dose (D_T) $D_T = \frac{1}{m_T}\int_{m_T} D\,dm$	Mean absorbed dose in an organ or tissue T of mass m_T.	gray (Gy) 1 J kg^{-1} = 1 Gy = 100 rad
Equivalent dose (H_T) $H_T = \sum_R w_R \cdot D_{T,R}$	Sum of the absorbed doses in the organ or tissue T caused by different radiation types R and weighted by the radiation weighting factors w_R recommended by ICRP.*	sievert (Sv) 1 J kg^{-1} = 1 Sv = 100 rem
Effective dose (E) $E = \sum_T w_T \cdot H_T$ $(\sum w_T = 1)$	Sum of the organ equivalent doses in all specified organs and tissues T of the body, weighted by the tissue weighting factors w_T recommended by ICRP.*	sievert (Sv)

* The last recommended values for the weighted factors w_R and w_T can be found in ICRP Publication 103. [27]

Table 2.4: Protection quantities. [20, 27]

personal dosimeters are calibrated in terms of these quantities. [26]

For area monitoring of penetrating radiation the operational quantity used as assessment of the effective dose is the ambient dose equivalent, H*(10). The H*(10) at a measurement point in a radiation field is defined[14] by ICRU as the dose equivalent that would be produced by the corresponding expanded and aligned field, in the ICRU sphere at a depth of 10 mm on the radius vector opposing the direction of the aligned field (i.e. the direction of the radiation incidence). [20, 27, 28]

To put it in a simpler form, the H*(10) can be seen as the dose equivalent that would be produced by a given radiation field at a depth of 1 cm of a 30 cm diameter sphere of tissue-equivalent material. Thereby, the H*(10) provides a conservative estimate of effective dose that one would receive staying at the measurement point. This is true in most situations of external radiation exposure, but it is not always the case, for example for exposures to high energy radiation fields with photons above 10 MeV. [27, 28]

Several area monitoring instruments available at CERN and used during this work, as the Automess 6150AD6/H (Geiger-Muller), measure the ambient dose equivalent rate dH*(10)/dt, i.e. the ambient dose equivalent per unit time.

The count rate (cps) was measured in the course of this work using the radiameter Thermo Electron FH 40G-L10 (proportional counter) coupled with the external probe FHZ 512 BGO[15]. Finally, the term "net count rate" is used to express that the count rate measured for the background has been subtracted from the gross count rate.

[14] The terms introduced by the definition are not described since they are out of the scope of the present work. More details can be obtained, for example, from ICRP publication 103 (2007) [27].

[15] Bismuth germanium oxide (BGO) scintillation cristal + Photomultiplier tube (PMT).

CHAPTER 3

Radioactivity at CERN

3.1 CERN Accelerator Complex

With a total tunnel extension of around 45 km, the CERN accelerator complex is mainly composed by a succession of accelerators (see Fig. 3.1) that increase the energy of particle beams before injecting them to the next accelerator in the chain until the LHC. Besides the LHC injection sequence, the accelerators deliver particle beams to a set of dedicated experiments that take place in parallel at CERN.

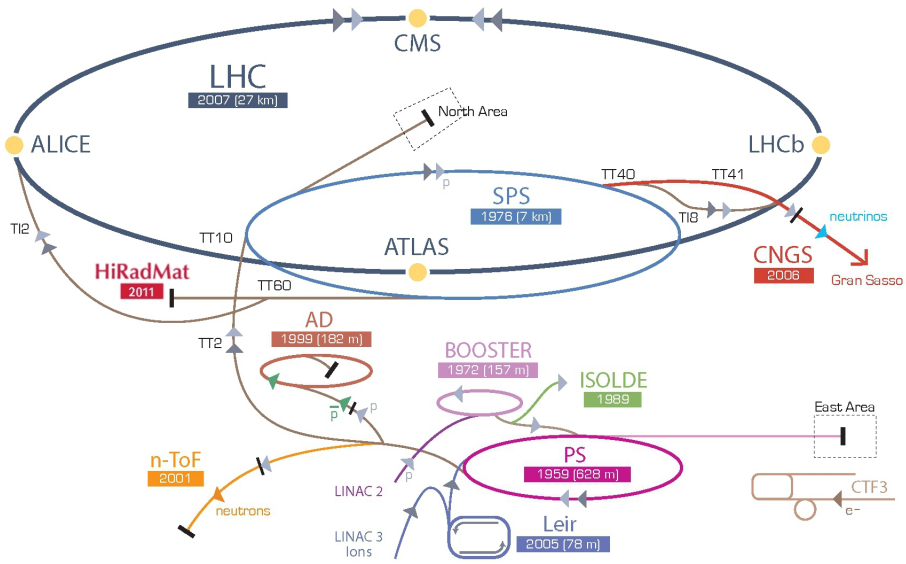

Figure 3.1: CERN accelerator complex.

The LHC numbers are well known and impressive. For protons, the injection from the SPS occurs at an energy of 450 GeV through two different injection points in such way that two proton beams circulate around the LHC in opposite direction to be, subsequently, accelerated to the energy of 4 TeV (2012). After the first long shutdown (LS1)

that will start in the first quarter of 2013, the goal will be to reach, within the first two years of operation, an energy of 7 TeV per beam and therefore p-p collisions with a center of mass of energy of 14 TeV and a collider luminosity[1] of 10^{34} cm^{-2}s^{-1}. At this stage, the phases of injection and ramp to the nominal energy of 7 TeV will take about 15 and 25 minutes, respectively [29].

The approximately 27 km long LHC ring is segmented into 8 arc sections and 8 straight sections (SS) called insertion regions (IR) (see Fig. 3.2), whose geometric centers[2] are known as interaction points (IP). The IP1, 2, 5 and 8 correspond to the four points where the two LHC beams can intersect, and hence, where the four experiments, ATLAS, ALICE, CMS and LHCb, are located. The corresponding IR1, 2, 5 and 8 are accordingly known as experimental insertion regions. Moreover, the two collimation systems[3] are hosted at IR3 and 7 while the radiofrequency (RF) cavities that keep the protons tightly bunched in the beams and provide accelerating voltage and energy gain to the beams are located at IR4. Finally, the beam dump extraction is done at IR6.

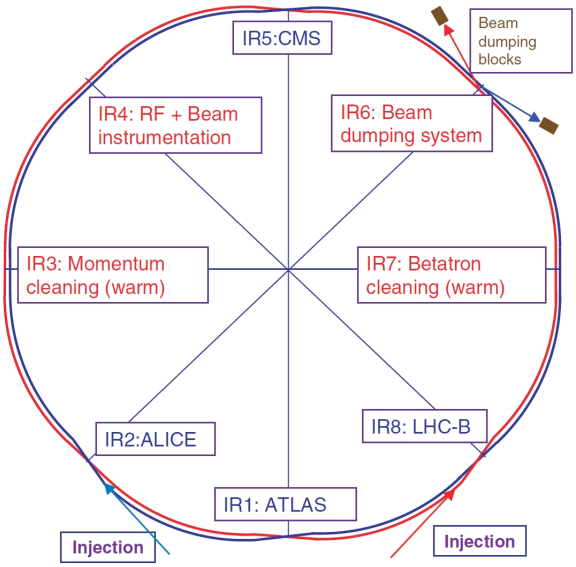

Figure 3.2: LHC layout. [29]

[1] 10^{34} events per cm^2 and per second (10^{27} cm^{-2}s^{-1} for Pb-Pb collisions). For a effective year of running (10^7 s) the corresponding integrated luminosity (integral of the luminosity over time) could reach 100 fb^{-1} (10^{41} cm^{-2}).

[2] Except for the IP8 that is shifted 15 RF wavelengths from the IR8 centre in direction of IP7 (15 RF wavelengths for the 400.8 MHz RF cavities $\simeq$ 11,2 m) [30].

[3] Maximum efficiency is achieved by implementing the betatron and momentum collimations in two separate regions [31]. The betatron collimation (IR7) removes halo particles with large transverse oscillation amplitudes (the transverse oscillations of the beam particles about the ideal orbit are known as betatron oscillations) while the momentum collimation (IR3) intercepts particles with large momentum offset. [30]

Under nominal operation conditions, each 7 TeV beam will contain 2808 bunches with an intensity of 10^{11} protons per bunch. At almost the speed of light, the 10^{14} protons per beam make more than 400 million revolutions around the machine during a typical beam lifetime of 10 hours. With all these large numbers, it becomes clear that beam losses around the LHC ring are inevitable and that the activation of its structure and surroundings, as also happens with the remaining accelerators in the complex, is an unavoidable side-effect of the research carried out at CERN. Therefore, at the end of their operational lifetimes as well as from the decommissioning of existing installations, some materials must be treated as radioactive waste. The radiological characterization of these materials is then required for their handling, transport and final elimination.

After more than 50 years of operation, substantial amount of radioactive accelerator components were accumulated and stored at CERN. The tunnel of the now dismantled Intersecting Storage Ring (ISR), an old accelerator which produced the world's first proton-proton and proton-anti-proton collisions in 1971 and 1981, respectively, is nowadays used as principal interim storage facility (see Fig. 3.3) of the radioactive waste coming from the whole CERN accelerator complex, until its final elimination towards French and Swiss repositories.

Figure 3.3: ISR interim storage.

The current flux of radioactive waste produced and stored at CERN is around 200 to 400 m^3 per year [32]. In addition, more than 500 radioactive sources are stored or used at CERN for dedicated experiments and calibrations. The Radiation Protection (RP) Group (part of the Occupational Health & Safety and Environmental (HSE) pro-

tection Unit) has the responsibility for radiation safety of these sources and has to ensure that the public and personnel at CERN are protected from the effects of ionizing radiation.

3.2 LHC Beam Loss Profile

Particles in the beam core escape continuously from the stability region (central orbit) and form around it a beam halo owing to small nonlinear components of the magnets guiding and focusing fields throughout the ring or due to several particle interactions: intra-beam, beam-residual gas or beam-beam interactions [33].

As described in the previous chapter, nuclear and electromagnetic interactions occur when beam particles collide with surrounding accelerator components, giving rise to particle showers (neutrons, protons, pions, kaons...) and resulting in local energy deposition (part of it inducing activation) and temperature increase of the struck material.

Despite the strong magnetic fields exerted by the magnets around the LHC ring, a fraction of particles diffuse outward from the beam core and get lost. The collimation system must protect the machine from these halo particles with a very high efficiency to prevent quenches[4] in the superconducting magnets, the most critical component in the accelerator. Unstable primary halo particles are first scattered by the primary collimator. The scattered particles (secondary halo) and the particle showers generated are then absorbed by secondary collimators and absorbers, and so on (multi halo collimation). The aim of this process is to confine a maximum number of the unavoidable losses to the cleaning insertions (with normal conducting (warm) magnets) and to reduce halo-induced backgrounds in the experiments regions (IR1, 2, 5, 8). The estimation is that about 30% of all the protons are lost in IR3 and IR7, making the cleaning insertions one of the most activated sections of the LHC [30, 35].

For nominal design parameters, an instantaneous loss of about 10^6 protons would be enough to quench a dipole magnet, i.e. with only 10^{-8} of the nominal beam intensity. The damage level for beam impact is estimated to be some 10^{10} protons, still four orders of magnitude below the nominal beam intensity of 10^{14} protons. Indeed, during colliding beam operation, the dominant beam losses are due to p-p collisions at the

[4]Phase transition of the magnet from the superconducting to normal conducting state. Protection systems were designed to dissipate the high energy stored in the superconducting magnet in case of a quench. Otherwise, the resistive zone of the magnet would increase its temperature to 1000 K in less than 1 s resulting in its destruction. [29, 34]

experimental insertion regions. For a nominal beam with a 10 h lifetime, the beam loss rate at IR1 and IR5, the two high luminosity insertions, is estimated to be $\sim 10^9$ protons per second and per beam, meaning that 99.9% of the beam losses must be captured by the collimation system. [29]

Fig. 3.4 shows a so-called loss map recorded by more than 3500 beam loss monitors (BLM), mostly ionization chambers, installed along the LHC ring.

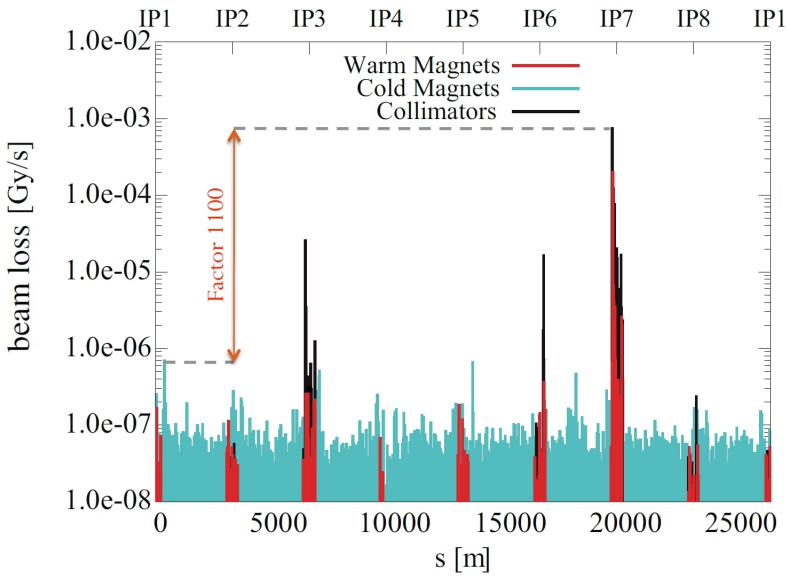

Figure 3.4: Loss map around the LHC ring for injection of Beam 1 (23.11.2009). (Offset without beam (background) subtracted). [36]

The higher beam losses are mostly at the beam cleaning insertions (IR3, IR7), as expected, but also at the other insertion regions, such as at the injection points and beam dumps. Distributed beam losses are also present in the arc sections, at least 1100 times smaller than the highest loss peaks found in the primary collimator in IR7, i.e. with a cleaning efficiency of around 99.9%, exactly as it should be.

3.3 The Proton Synchrotron (PS)

Built in the late 1950s, the PS accelerator reached its nominal energy of about 25 GeV for the first time in November 1959, being then, but for only a few months, the world's highest energy particle accelerator. In the first years, the PS supplied physics experiments with secondary beams produced from internal targets and later extracting directly the primary beam from the machine to external targets. Afterward, the PS started to feed more powerful accelerators, first the ISR in 1970, followed by the SPS in 1976 and later the LEP in 1989. [37, 38]

Over the years, the PS has been subject to several modifications and upgrades. Its beam intensity increased by several order of magnitude (see Fig. 3.5) and it accelerated many different kinds of particles: p, $\overline{p}$, e^-, e^+, light and heavy ions [38].

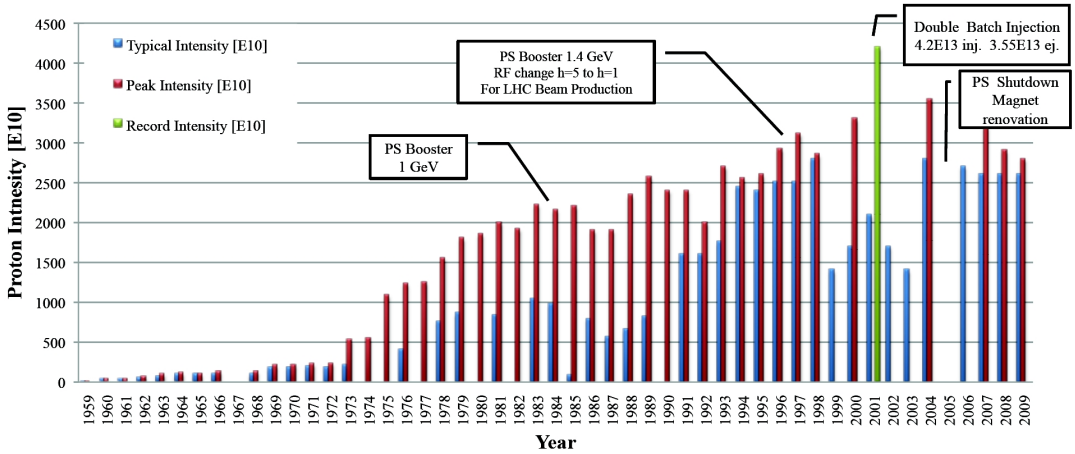

Figure 3.5: PS proton intensity (protons per pulse) evolution over 50 years. [37]

Nowadays the PS accelerates mostly protons delivered by the Proton Synchrotron Booster (PSB) at 1.4 GeV to be afterwards injected at 14 GeV into the SPS or to feed a set of experiments shown in Fig. 3.6.

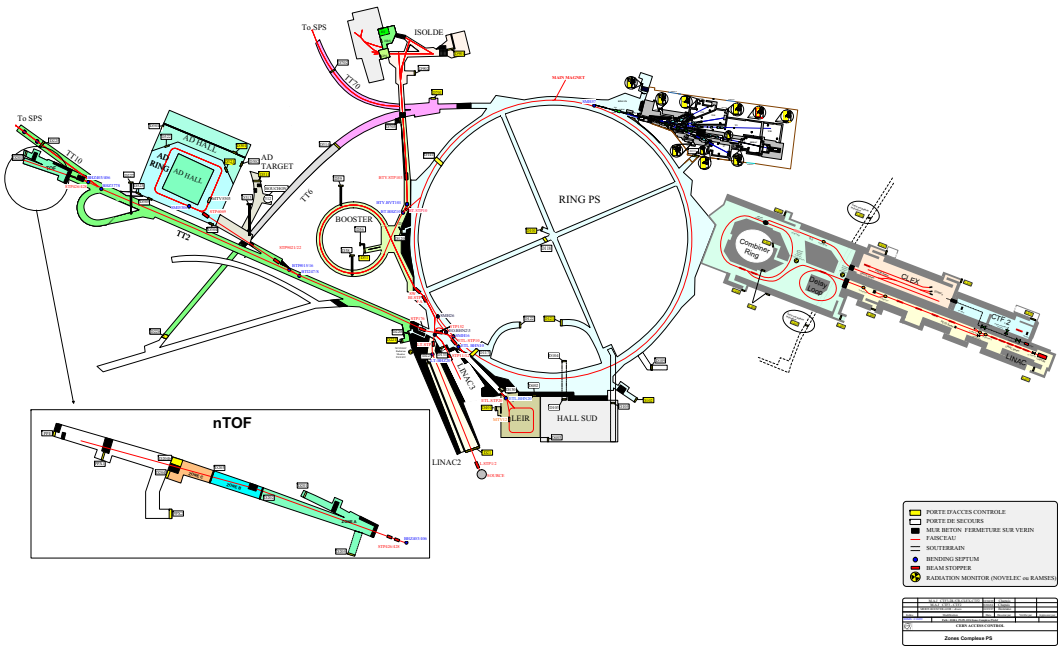

Figure 3.6: The PS complex. [39]

With a circumference of 628 m, the PS tunnel is made up of 100 magnet units (MUs) of 4.4 m length, that combine dipole and quadrupole magnetic fields in one

magnet. The straight sections located between the successive MUs, composed by 80 short straight sections of 1.6 m and 20 long straight sections of 3 m, are used for RF cavities, beam observation stations, injection and extraction elements, and auxiliary magnets (quadrupoles, sextupoles and octupoles). [37]

3.4 PS Beam Loss Profile

Regarding to beam loss effects leading to elevated above-ground dose rate levels, the PS can be seen as the weak point of the CERN's accelerators chain given that both SPS and LHC are well below the ground, in opposition to the PS that is close to ground level. The thickness of the shielding above the PS ring varies between 3.2 m and 4.8 m and consists in 50 cm of concrete (the tunnel ceiling) and the remainder mostly of soil [40].

The consequences of the beam losses are numerous. When the beam is operating, the losses give rise to the prompt radiation[5] which increases equipment damage and failure rates on electronic systems. Secondaries created by the primary beam losses contribute to the activation of surrounding materials such as accelerator components but also soil, groundwater and air that can afterwards be released to the environment by the ventilation system. The stray radiation[6] propagates through the weak part of the shielding of the accelerator, commonly the roof since the vertical walls are generally thicker, and may reach the surface for machines close to the ground level. On the other hand, during beam off, the larger have been the losses, the greater the induced radioactivity in the machine and the personnel dose during maintenance works.

For dose rate monitoring purpose, radiation surveys of the PS complex are held periodically. In the PS tunnel, the surveys are carried out with an Automess AD6 used at a lateral distance of 40 cm, upstream and downstream from the vacuum chamber of each straight section. The AD6 measures the ambient dose equivalent rate which depends on the materials activation that in turn is related with the beam losses. Hence, the PS ring surveys give an idea on the location where the losses occur around the tunnel. Fig. 3.7 shows the ambient dose equivalent rate along the ring at 40 cm from the vacuum chamber, normalized to 32 hours after the shutdown of November 2011.

[5]Prompt, instantaneous or direct radiation is the radiation due to the beam interaction with the surrounding matter. Is produced only when the accelerator is turned on, in opposition to the residual radiation coming from induced activity.

[6]Radiation leakage or stray radiation is the penetrating component of the prompt radiation, mainly neutrons but also photons and muons, emitted into the environment through the weak parts of the shielding.

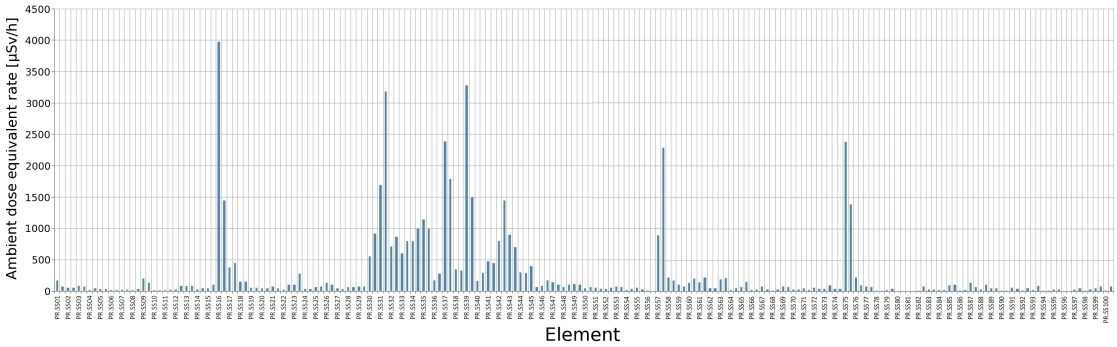

Figure 3.7: Radiation survey around the PS ring normalized to 32 h after beam stop. (Adapted from [41])

Analyzing Fig. 3.7, one can identify 6 high radiation areas (> 2 mSv/h): SS16, SS31, SS37, SS39, SS57 and SS75, plus one with almost 1.5 mSv/h, the SS42. Almost all of them are associated with the injection into and the ejection from the PS. During the ejection by the Continuous Transfer (CT) process, the beam is sliced horizontally in 5 portions on the electrostatic septum SEH31 (SS31) before being extracted by the magnetic septum SMH16 (SS16). Due to this type of extraction, two beam loss areas occur in SS37 and SS39. The magnetic septum SMH42 (SS42) is used to inject the beam from the PSB into the PS while the magnetic septum SMH57 (SS57) extracts protons to the East Hall (see Fig. 3.8). Finally, a loss peak occurs in SS75 where a fast wire scanner is used to measure vertical profiles of the beam. Nevertheless, the description of the beam extraction is outside the scope of this work (details can be found, for example, in [37]).

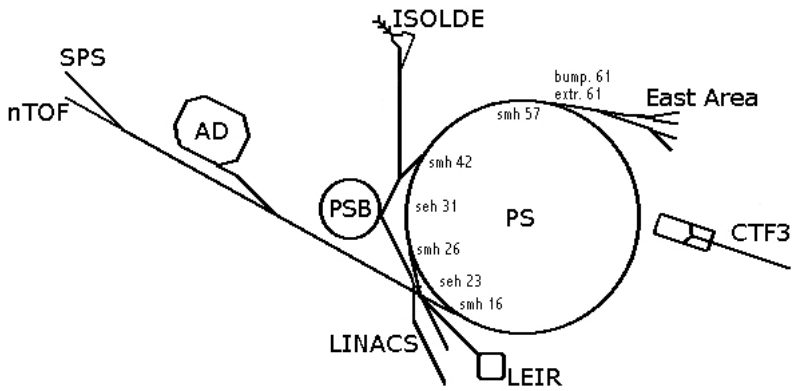

Figure 3.8: Septa map and the PS complex. (Adapted from [42])

Beam losses[7] up to 6% occur in the injection region (SS42) of the PS while the ex-

[7]For a beam injected from the PSB at 1.4 GeV kinetic energy and intensity of about 10^{12} protons per second. [43]

traction of the beam to several experiments results in losses[8] of 2 to 10% depending on the extraction mechanism used: the Multi-Turn Extraction (MTE) which concentrated almost all losses in the magnetic septum SS16 or the older Continuous Transfer extraction, aforementioned, that causes beam losses of about 10% distributed over several regions downstream from the electrostatic septum SS31 [43].

3.5 The PS Chilled Water Pipes

The PS tunnel is air-conditioned to provide temperature and humidity stabilization. Furthermore, to prevent the entrance of atmospheric dust, a small air overpressure is kept in the tunnel [44]. A uniform control of the temperature along the ring is provided by heating and cooling pipes, installed in 1957 on the top of the tunnel over its entire length (see Fig. 3.9 and 1.1).

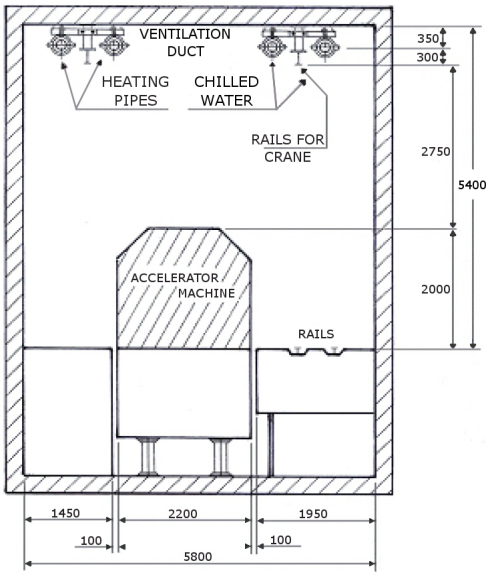

Figure 3.9: Scheme of the iced water pipes location in the PS tunnel. [45]

Attending to the normal technical lifespan of piping and due to corrosion problems, the iced water pipes replacement started in the 2000-2001 long shutdown, 43 years after their installation. The PS complex has the longest run period among all the CERN accelerators meaning that the access to the PS cooling stations for maintenance is limited to the minimum [46]. As a consequence, the exchange of the iced water pipelines had to be extended to the long shutdowns that followed, until 2004.

[8]For an extraction from the PS at a kinetic energy of 14 GeV and intensity of about 10^{12} protons per second. [43]

According to measurements carried out after the dismantling of the last pipeline section done during the shutdown 2003-2004, the count rate (BGO) at contact for each 4 to 6 meters long pipe varies significantly, being a function of their former location inside the tunnel. Fig. 3.10 presents a graph produced in 2004 of the count rate measurements at contact for 43 tubes (only some of them were represented in the graph). The highest count rate values of the batch of tubes obtained in this last dismantlement campaign, correspond to the pipes situated in the vicinity of the electrostatic septum SEH31 [45] and the magnetic septum SMH42, as expected due to the high beam losses in these areas.

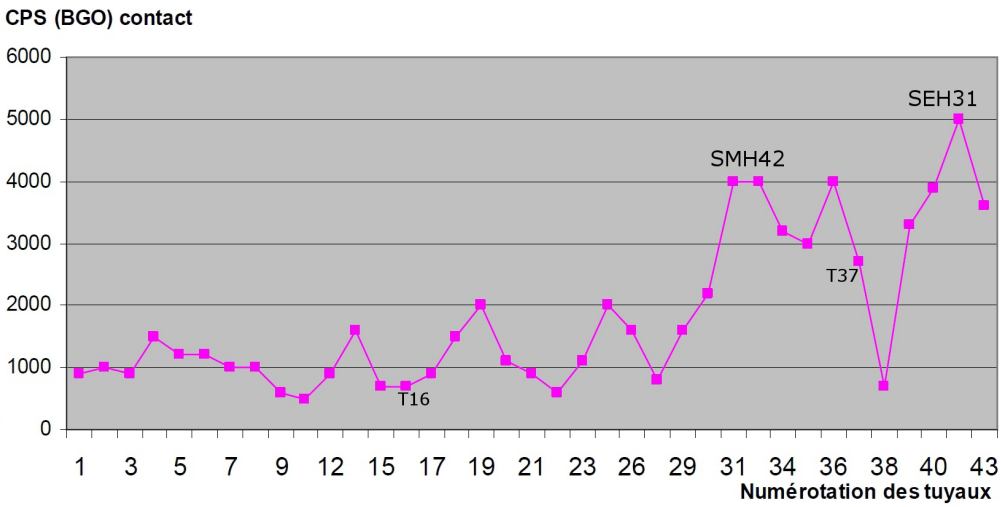

Figure 3.10: Count rate measurement (February 2004). (Adapted from [45])

Using the results of the gamma spectrometry analysis of samples from the pipes T16 and T37 (see Tab. 3.1), and the count rate measurements of these two pipes (see Fig. 3.10), one can conclude that the ratio between the total specific activity and the count rate would be, at that time, of the order of 0.01 Bq g^{-1} cps^{-1}. Moreover, applying the exponential decay law (see Eq. 2.1.4) to the γ-spectrometry results of the pipe T37 (see Tab. 3.1), one can infer that its total specific activity, after a cooling time of about 8 years, will be around 5 Bq g^{-1}, and that twice this value can be expected for the most activated tubes found during this dismantling campaign (see Fig. 3.11).

A final word regarding the location of the chilled water pipeline relative to the PS beam level: approximately 2.5 to 3 m separates the beam line level from the pipeline, meaning that their activation must have occurred through interactions with particle showers rather than directly with primary protons.

The activation by secondary hadrons can be divided into two main components [9], one due to spallation reactions by high energy secondary hadrons and another one

Sample origin	Date of measurement	Radioelements	Half-life [y]	Specific activity [Bq g^{-1}]	Error (%)
Acier Tuyauterie (T 37)	03.03.2004	^{46}Sc	0.229	0.159	29.1
		^{51}Cr	0.076	0.578	44.4
		^{54}Mn	0.855	14.6	10.3
		^{57}Co	0.744	0.0496	37
		^{59}Fe	0.122	0.835	15.4
		^{60}Co	5.271	15.6	8.2
Acier Tuyauterie (T 16)	03.03.2004	^{46}Sc	0.229	0.072	40.9
		^{54}Mn	0.855	4.06	11
		^{60}Co	5.271	3.06	9.1

Table 3.1: Gamma spectrometry results from pipes T16 and T37. [45]

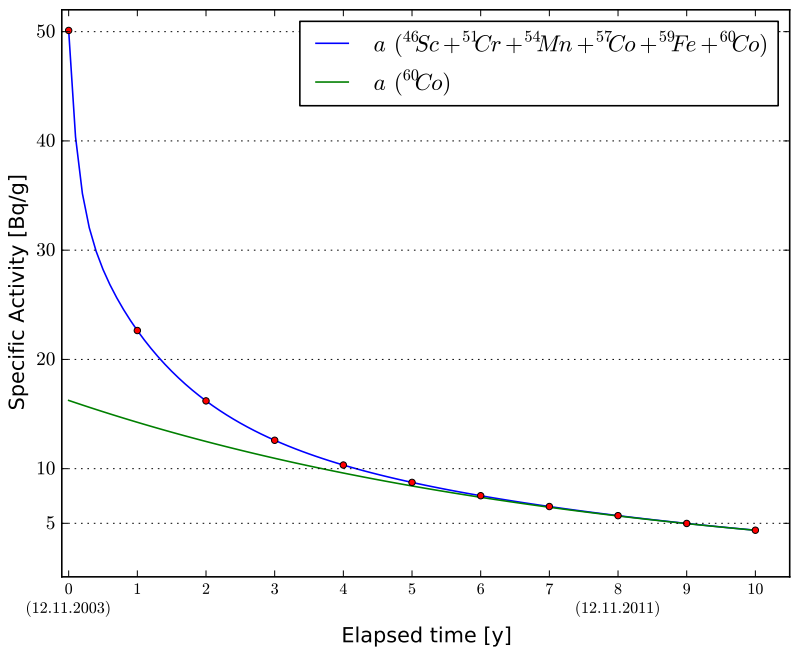

Figure 3.11: Decay of the specific activity of the sample T37 for a cooling time of 10 years after the machine shutdown (12.11.2003). The blue line corresponds to the total specific activity and the green to the specific activity of ^{60}Co only. (Based on the gamma spectrometry results from tab. 3.1)

due to radiative capture reactions particularly of thermal neutrons. Furthermore, a feature of high energy hadron showers is the concentration of energetic particles mainly around the primary beam axis, irrespective of the particle identity [15]. Therefore, in the case of the chilled water pipeline, laterally away from the beam line, it is acceptable to conclude that most of the interactions must have occurred with the neutron component of the hadronic showers.

Specific Activity and Total Activity
The specific activity of the radionuclides present in the material exceeds the CERN exemption limits (LE) which are taken from the Swiss Ordinance on Radiation Protection (Annex 3 Column 9) [50].*   AND   The total activity of the material exceeds the CERN exemption limits ($LE_{abs} \equiv$ LE expressed in Bq).
Dose Rate (DR)
The ambient dose equivalent rate measured in 10 cm distance of the material exceeds 0.1 μSv h^{-1} after subtraction of the background.   [For solid β and γ emitters†: the materials are classified as slightly radioactive (0.1 μSv h^{-1} $\leq$ DR $\leq$ 10 μSv h^{-1}), radioactive (10 μSv h^{-1} $\leq$ DR $\leq$ 100 μSv h^{-1}) and highly radioactive ($\geq$ 100 μSv h^{-1})]
Surface Contamination
The surface contamination‡ of the material exceeds 1 Bq cm^2 in case of unidentified β and γ emitters and 0.1 Bq cm^2 in case of unidentified α emitters. If the radionuclides are identified then the guidance values§ (CS-values) can be used jointly with the summation rule [50].

* For example: $LE_{Co60} = 1 \times 10^3$ Bq kg^{-1}, $LE_{Mn54} = 1 \times 10^4$ Bq kg^{-1}, $LE_{Fe55} = 3 \times 10^4$ Bq kg^{-1}. In the most common case of a nuclide mixture, the summation rule specified in Annex 1 of [50] should be applied.

† β and γ emitters are the most common radioactive waste produced at CERN. [32]

‡ Surface contamination averaged over 100 cm^2 (wipe test of 100 cm^2 area).

§ Annex 3 Column 12 of [50].

Table 3.2: CERN's exemption limits for radionuclides of artificial origin. [48–50]

3.6 Elimination Pathways of Radioactive Waste from CERN

As an intergovernmental organization recognized by the two Host States, CERN has the warrant to establish its own safety policy for the exercise of its functions [47]. The Safety Code F outlines CERN's radiation protection rules that guarantee radiological safety at a level at least equal to that present in both Host States [48]. Thereby, the CERN's safety standards ensure the protection of people and the environment against ionizing radiation at the "As Low As Reasonably Achievable" (ALARA) level.

In agreement with the Safety Code F and as summarized in [49], a material is considered to be radioactive if it fulfils at least one of the 3 requirements stated in Tab. 3.2. A radioactive material which is no longer of use at CERN is considered as radioactive waste [48]. The life cycle of the radioactive waste at CERN is presented in Fig. 3.12.

In accord with the tripartite agreement signed in 2011 between CERN and its two Host States, different elimination pathways are available for the radioactive waste produced on site and shall be selected according to a principle of "fair share" taking into account the eliminated mass, activity and radiotoxicity of the waste.

If exempted from the application of Safety Code F (see Tab. 3.2), the waste can be eliminated as "Free-release" in Switzerland (elimination pathway not existing in France). On the other hand, if the waste activity or surface contamination are above

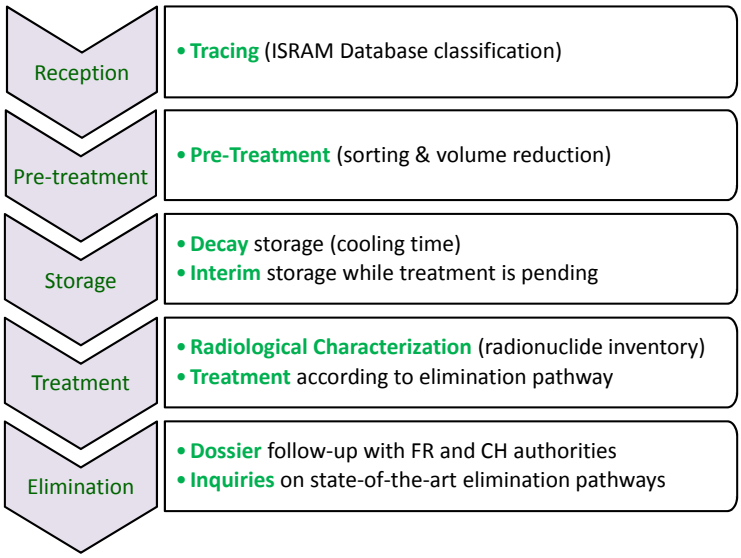

Figure 3.12: Life cycle of CERN radioactive waste. (Adapted from [51])

the exemption limits and below the ANDRA acceptance criteria, then the elimination towards France, as TFA waste, can be the solution[9]. Medium level waste shall be eliminated in France (as FMA (Faiblement ou Moyennement Actifs) waste) or in Switzerland according to the principle of fair share.

Based on the rough analysis of the data collected in 2004 during the last dismantling phase of the chilled water pipeline inside the PS (see Sec. 3.5) and taking into account that the CERN exemption limit for ^{60}Co is equal to 1 Bq g^{-1} (see Tab. 3.2), it becomes clear that the most probable elimination pathway of the batch of PS pipes, after their interim storage of almost 8 years near building 573, should be as TFA radioactive waste towards the French final repository: Centre de Stockage des déchets Très Faiblement Actifs (CSTFA) located at Morvilliers in the Aube district.

3.7 ANDRA Radiological Acceptance Criteria

For the acceptance of a batch of radioactive waste in the ANDRA's TFA storage center, different criteria must be fulfilled, such as:

[9]The radioactive waste (déchets nucléaires) produced in a ZDN (Zone à Déchets Nucleaire) can be classified as TFA (Très Faiblement Actif), FA (Faiblement Actif), MA (Moyennement Actif) and HA (Hautement Actif) [52]. The majority of the radioactive waste at CERN has a very low level of activity [32]. The activity of TFA waste is generally below 100 Bq g^{-1} [53].

French designation	Definition
Colis	Primary package (container + conditioned waste) or single piece without packaging. The container must allow individual handling without dispersion and contamination risks.
Lot	Batch of primary packages which origin and characteristics allows the elaboration of a unique acceptation dossier.
IRAS	Indice Radiologique d'Acceptation en Stokage. The radiological index for disposal acceptance restricts the upper limit of the specific activity of the radioactive waste in function of its radionuclide inventory.
Classe TFA	TFA class (0, 1, 2, 3) listed by radionuclide and according to its level of radiological toxicity (with the TFA class 3 corresponding to the radionuclides with lower toxicity).
Activité massique forfaitaire	Majorant value of the total specific activity that can be applied to a primary package to avoid its exact value calculation. In such case the value of the IRAS factor of the primary package must be below 0.5.
Seuil de déclaration	Reporting threshold of the specific activity listed by radionuclide. All the radionuclides with higher specific activity than the reporting threshold must be declared and used for the IRAS computation.
Limite de déclaration forfaitaire (LDF)	Reporting limit of the specific activity listed by radionuclide. All the radionuclides must have a specific activity below the LDF to be possible to use a majorant value of total specific activity.

Table 3.3: ANDRA's technical terms.

- Radiological acceptance criteria;
- Physicochemical acceptance criteria;
- Treatment and conditioning rules.

Only the radiological criteria are described in order to restrict the discussion to the main subject of this thesis. A set of definitions stated by ANDRA and used throughout the approval process of radioactive waste to the TFA repository are presented in Tab. 3.3.

3.7.1 IRAS Factor

The IRAS factor of a primary package is defined mathematically by Eq. 3.7.1

$$IRAS_{colis} = \sum_i \frac{a_i}{10^{Classe_i}}, \tag{3.7.1}$$

Radionuclide	Half-life [y]	TFA class	Reporting threshold [Bq g^{-1}]	LDF [Bq g^{-1}]
^{60}Co	5.271	1	0.1	-
^{55}Fe	2.744	3	10	-
^{54}Mn	0.855	1	0.1	-
^{3}H	12.32	3	1	10

Table 3.4: TFA class, reporting threshold and LDF of some radionuclides. (Data from ANDRA)

where a_i and $Classe_i$ are the specific activity (Bq g^{-1}) and the TFA class of the radionuclide i, respectively.

The Tab. 3.4 presents a short list of radionuclides extracted from data provided by ANDRA.

The IRAS$_{\text{lot}}$, i.e. the IRAS of the batch of primary packages is obtained computing the mass weighted average of the IRAS primary package (see Eq. 3.7.2).

$$IRAS_{lot} = \frac{\sum_j M_j \cdot IRAS_j}{\sum_j M_j} \tag{3.7.2}$$

where $IRAS_j$ and M_j are the IRAS and the mass of the primary package j, respectively.

Finally, for the waste acceptance at the TFA disposal facility, the IRAS$_{\text{lot}}$ of the batch of primary packages must be below 1 and the corresponding IRAS of each primary package below 10.

CHAPTER 4

Strategy for Radiological Characterization

The PS chilled water pipes were stored close to building 573 for about 7 years (see Fig. 4.1) until 2011. Before the process of characterization might take place, the pipes were pre-conditioned according to the needs of this process and to ANDRA requirements.

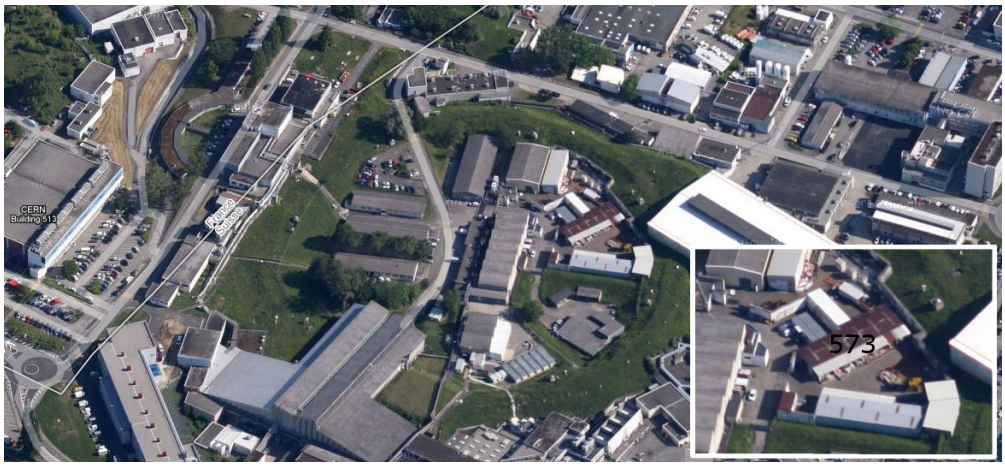

Figure 4.1: Location of building 573.

4.1 Pre-conditioning

The steps involved in the pre-conditioning process, shown in Fig. 4.2, are as follows:

- Tube cutting: ANDRA requirements and the dimensions of the ANDRA contain-

ers (L = 1326 mm, W = 1034 mm, H = 967 mm) imposed that the pieces had to be stored vertically inside the containers and consequently had to have around 85 cm in length, roughly 10 cm below the container height and corresponding to 7 pieces of equal length for the 6 m long tubes. For this purpose, an enclosed area was built in order to confine most of the contamination due to rust released by the tubes during the cutting process;

- Compaction: since the price of the waste storage at the TFA repository is a function of volume of waste and not of its mass, the pipes had to be compacted before being conditioned inside the ANDRA containers. This was done by a COPEX press machine that, with a maximum pressure around 300 bar, compacted the 85 long pieces to a maximum thickness of about 3 cm, depending on the former diameter of the pieces (ranging from 8 to 22 cm);

- Mass measurement: the pieces were weighted one by one with a pallet truck scale with an accuracy of the order of 0.1 kg;

- Count rate measurement: performed at contact at the center of each piece and searching for hot spots[1] along them, using the radiameter FH 40 G-GL equipped with a FHZ 512 BGO external probe. Pieces with hot spots and/or with non-standard shapes[2] had to be separated from the other pieces in order to be individually characterized. Finally, pieces with count rates known as "reference values" (100, 200, 300... cps) were selected and separated for the measurement of their activity, as outlined in the section below.

4.2 Radiological Characterization

The outlines of the characterization process used for the chilled water pipes from the PS accelerator are shown in Fig. 4.3.

As described in the next chapter, FLUKA and JEREMY computer codes were used jointly with all the inputs necessary to get, as output, the radionuclide inventory of the PS pipes and to validate one of the processes of normalization used during the characterization. As it will be seen later on, the list or inventory of radionuclides obtained from JEREMY for the PS pipes is given for a loss beam rate of 1 primary particle per second, meaning that this gross data had to be normalized in order to be used for the

[1] Higher activated region, hence presenting a higher dose or count rate.
[2] A standard piece was considered as being an approximately 85 cm long piece of tube.

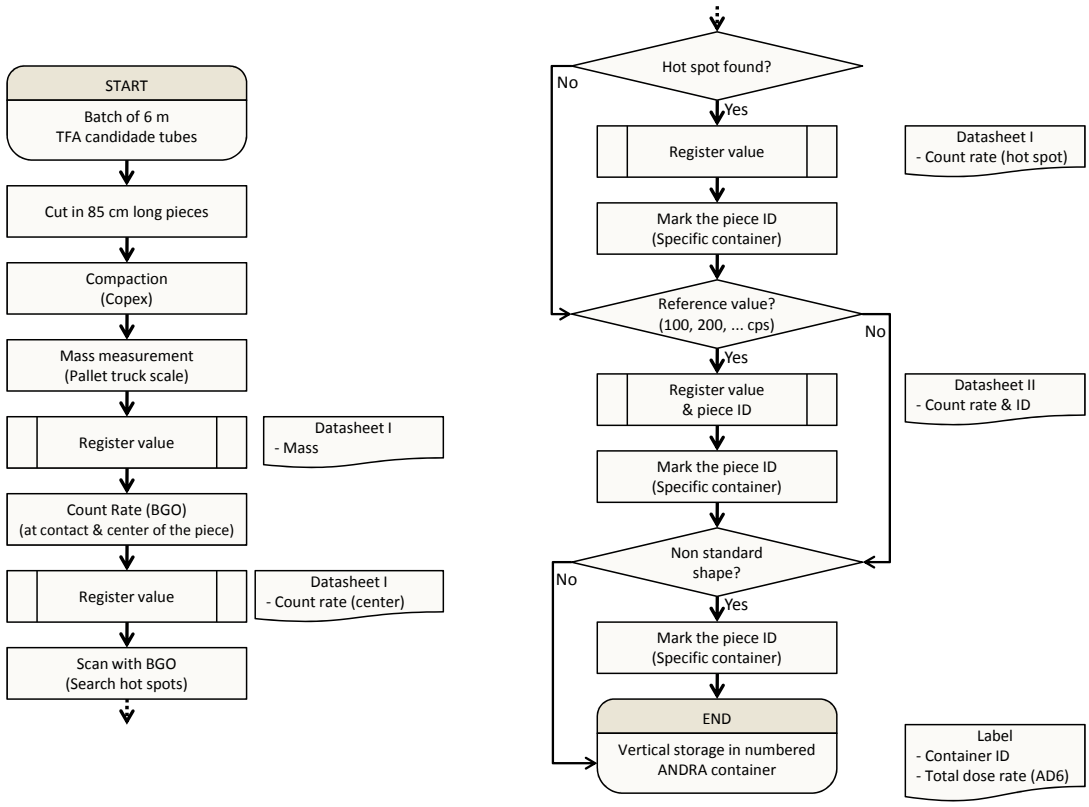

Figure 4.2: Pre-conditioning process.

IRAS computation described in the previous chapter. Two different approaches for the normalization were tested in this work (see Fig. 4.4), in order to compare and evaluate the operationality of both methods for future projects. As a result of the different normalization methods, two values for the IRAS factor were obtained. To be conservative in respect to the activation level of the batch of tubes, the highest IRAS factor must be used in the document prepared for the acceptance of the PS pipes at the ANDRA repository.

Both normalizations are described in the next two subsections. For their validation, approximately[3] 70 m of pipeline, i.e. about 85 pipe pieces, were pre-conditioned according to the steps described in Fig. 4.2. For the second method of normalization an additional measurement of the dose rate at contact of all the pipe pieces was performed using the dosimeter Saphymo SCINTO (NaI scintillation crystal). In spite of being an old instrument, the SCINTO was preferred to the detriment of the AD6 since its measuring range is more appropriate for low dose rates (from 40 nSv h^{-1} for the SCINTO vs. 100 nSv h^{-1} for the AD6).

[3]The expected total length of pipeline corresponds to twice the circumference of the PS ring, i.e. 1256 m. Approximately 5.5% of pipeline was then pre-conditioned for validation.

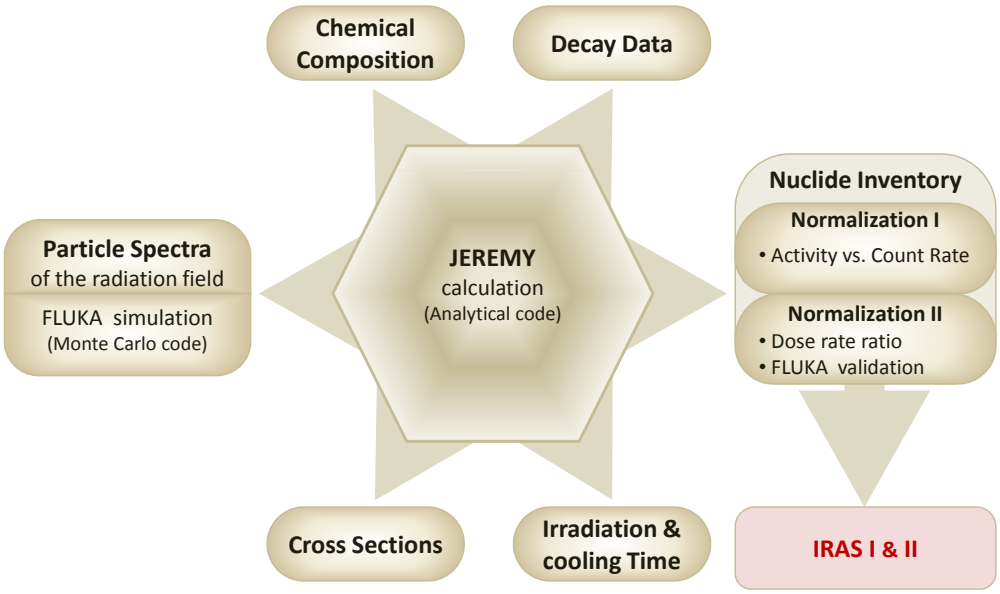

Figure 4.3: Radiological characterization process.

4.2.1 Specific Activity vs. Count Rate

This method is based on the linear relationship between the dose or count rate measured from a radioactive material and its specific activity. The latter could be obtained collecting and sending a sample of the material to the γ-spectroscopy laboratory, or using a field deployable gamma spectrometer: In Situ Object Counting System (ISOCS) or a 4π total gamma measurement chamber (RADOS RTM661/440) provided that the nuclide inventory is known[4] (see Fig. 4.5).

The Fig. 4.6 shows the specific activity vs. count rate relationship obtained with the measurements (RTM and BGO) of a total of 17 pipe pieces. As seen in Fig. 3.11 and confirmed with recent gamma spectrometry measurements, after 7 years of cooling time, ^{60}Co is the only gamma emitter measurable in the PS pipes. Therefore, the total activity obtained from the RADOS RTM measurements was considered as being exclusively from ^{60}Co. The presence of ^{55}Fe was also predicted and confirmed sending samples to the "haute école du paysage, d'ingénierie et d'architecture de Genève" (HEPIA), as discussed in the chapter 6.

The relationship obtained between the specific activity of ^{60}Co a_p^{Co60} for each piece

[4] All three methods (γ-spectroscopy, ISOCS and RADOS) were used and compared, obtaining a good match of the measured activities. Nevertheless, the RADOS RTM661/440 was preferred and used to implement this method of normalization since it is much faster at delivering results (only few seconds with the pipe piece inside the 4π gamma chamber were enough to yield its total activity with a precision better than 6%) and also because the nuclide inventory was well known.

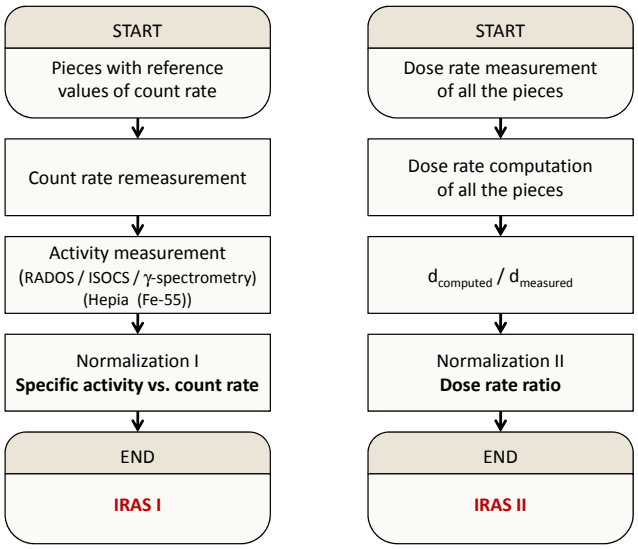

Figure 4.4: Normalization methods.

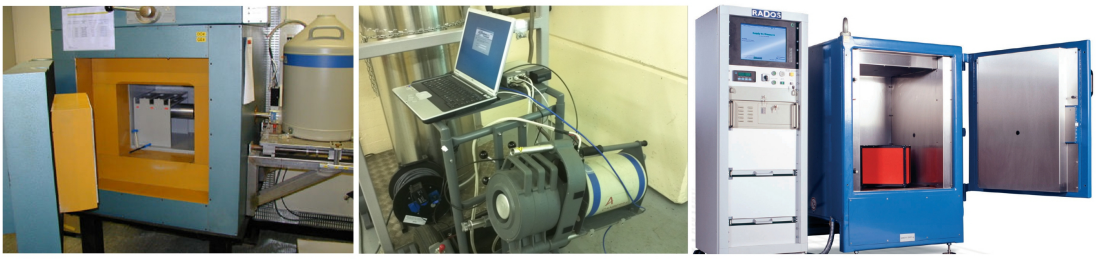

Figure 4.5: From left to right: γ-spectrometer (Ge detector), in situ γ-spectrometer (Ge detector) and 4π gamma counter (6 plastic scintillation detectors).

p and their respective count rates CR_p is expressed through Eq. 4.2.1

$$a_p^{Co60} = \frac{A_p^{Co60}}{M_p} = 0.00736 \times CR_p + 0.0148, \tag{4.2.1}$$

where A_p^{Co60} and M_p are the activity of ^{60}Co and the mass of the piece p, respectively.

Then, from Eq. 3.7.1, the primary package (colis) ^{60}Co activity A_{colis}^{Co60} and the corresponding ^{60}Co IRAS factor could be obtained using

$$IRAS_{colis}^{Co60} = \frac{1}{10^{cl_{Co60}}} \frac{\sum_p M_p \frac{A_p^{Co60}}{M_p}}{M_{cont} + \sum_p M_p} = \frac{1}{10^{cl_{Co60}}} \frac{\sum_p A_p^{Co60}}{M_{cont} + \sum_p M_p} = \frac{1}{10^{cl_{Co60}}} \frac{A_{colis}^{Co60}}{M_{colis}}, \tag{4.2.2}$$

where the mass of the colis M_{colis} includes the container mass M_{cont}, in the case of the container not be recovered after sending it to the final repository.

To get the total $\text{IRAS}_{\text{colis}}$, i.e. the IRAS factor of the primary package taking into

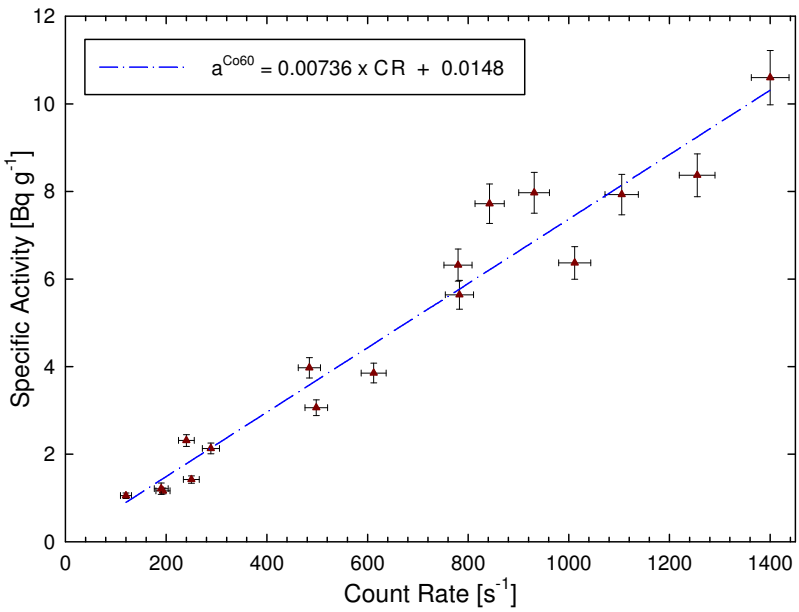

Figure 4.6: Specific activity (RADOS RTM661/440) vs. count rate (FHZ 512 BGO) data and respective linear regression (R^2 = 0.9499).

account the complete nuclide inventory, the factor $IRAS_{jer}^{Total}$ / $IRAS_{jer}^{Co60}$ coming from the JEREMY code (see chapter 5) has to be applied as shown in Eq. 4.2.3

$$IRAS_{colis}^{Total} = \frac{IRAS_{jer}^{Total}}{IRAS_{jer}^{Co60}} \frac{1}{10^{cl_{Co60}}} \frac{A_{colis}^{Co60}}{M_{colis}}. \tag{4.2.3}$$

Finally, from Eq. 3.7.2, the total IRAS of the batch of primary packages (lot) can be obtained using

$$IRAS_{lot} = \frac{\sum_{colis} M_{colis} \frac{IRAS_{jer}^{Total}}{IRAS_{jer}^{Co60}} \frac{1}{10^{cl_{Co60}}} \frac{A_{colis}^{Co60}}{M_{colis}}}{\sum_{colis} M_{colis}} = \frac{IRAS_{jer}^{Total}}{IRAS_{jer}^{Co60}} \frac{1}{10^{cl_{Co60}}} \frac{\sum_{colis} A_{colis}^{Co60}}{\sum_{colis} M_{colis}}. \tag{4.2.4}$$

The results of this method are presented in the chapter 6.

4.2.2 Dose Rate Ratio

The second method of normalization is based on the analytical computation of the dose rate of each pipe piece, assuming that the pieces are homogeneously activated. The dose rate d at the measurement point (x^m, y^m, z^m) is obtained by integrating the dose rate generated by the specific activity of each radionuclide present in the pipe piece over its entire volume using Eq. 4.2.5. Since the pieces were previously com-

pacted during the pre-conditioning phase, their geometry was approximated by a rectangle parallelepiped of 85 cm x 25 cm x 1 cm, as shown in Fig. 4.7.

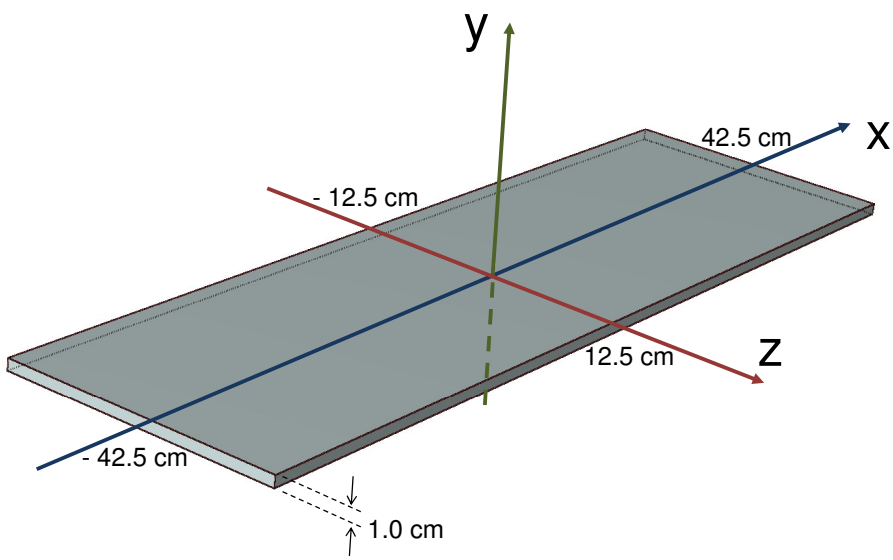

Figure 4.7: Geometry approximation of the compacted pipe pieces.

$$d(x^m, y^m, z^m) = \sum_i \sum_j \int_V dx\, dy\, dz\, p(E_\gamma^{j,i})\, d(E_\gamma^{j,i}, x, y, z)\, a_i\, \rho\, e^{-\mu(E_\gamma^{j,i})\,\lambda(x,y,z)} \tag{4.2.5}$$

The three dimensional integral is computed separately for each gamma energy j of each radionuclide i present in the pipe piece and then added to get the total dose rate at the point (x^m, y^m, z^m).

with

- $\lambda(x, y, z)$ [cm], the path length inside the pipe piece for a photon emitted at the position (x, y, z) (see Fig. 4.8);
- $\mu(E_\gamma)$ [cm^{-1}], the linear attenuation coefficient of a photon of energy E_γ, inside the pipe piece;
- ρ [g cm^{-3}], the density of the pipe;
- a_i [Bq g^{-1}], the specific activity of the radionuclide i homogeneously distributed over the pipe piece (for a unit loss, i.e. one beam particle lost per second, in the case of using the specific activity directly from the JEREMY code);

- $d(E_\gamma, x, y, z)$ [Sv h^{-1} / γ s^{-1}], the dose rate at the measurement point (x^m, y^m, z^m) due to the emission of one photon per second of energy E_γ at the position (x, y, z), assuming no attenuation due to interactions with matter;
- $p(E_\gamma)$, the emission probability per decay of a photon with energy E_γ.

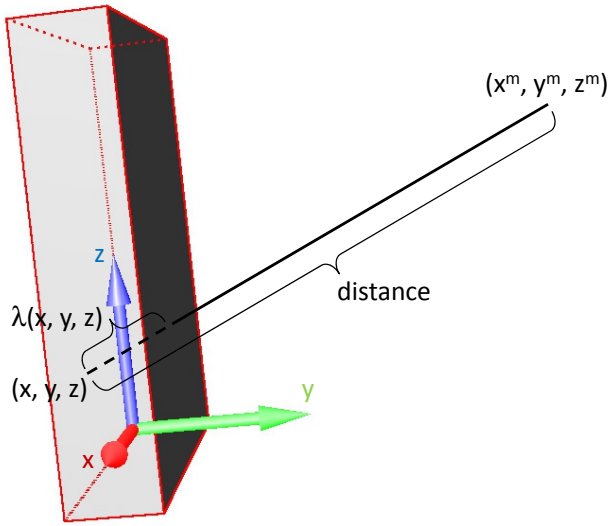

Figure 4.8: Distance between emission and measurement points.

The distance between the emission point (x, y, z) inside the pipe piece and the measurement point (x^m, y^m, z^m) (see Fig. 4.8) is given by

$$distance = \sqrt{(x^m - x)^2 + (y^m - y)^2 + (z^m - z)^2}. \tag{4.2.6}$$

Hence, the path length of each emitted photon can be written as

$$\lambda(x, y, z) = \frac{y^{max} - y}{y^m - y}\sqrt{(x^m - x)^2 + (y^m - y)^2 + (z^m - z)^2} \tag{4.2.7}$$

for $0 \leqslant x \leqslant x^{max}$, $0 \leqslant y \leqslant y^{max} < y^m$ and $0 \leqslant z \leqslant z^{max}$, where x^{max}, y^{max} and z^{max} correspond to the width, thickness and length of the pipe piece, respectively, as plotted in Fig. 4.8.

The energy dependent linear attenuation coefficient of electromagnetic radiation in matter was computed[5] from [8]

[5]The approximation used for the total attenuation coefficient includes the photoelectric effect that corresponds to the first term of Eq. 4.2.8, Compton absorption and scattering (second term) and pair production (third term).

$$\frac{\mu}{\rho}(E_\gamma, A, Z) = 1.8 \times 10^{-5} \frac{Z^{4.05}}{A} (10E_\gamma/1\text{MeV})^{-3} + 0.1267 \frac{Z}{A} (E_\gamma/1\text{MeV})^{-0.45} + 3.52 \times 10^{-4} \frac{Z^2}{A} (3.11 \ln (3.92\, E_\gamma/1\text{MeV}) - 8.07) \ \text{g}^{-1}\text{cm}^2 \tag{4.2.8}$$

where ρ, A and Z are the density, atomic mass and atomic number of the pipes material, respectively.

On its part, the dose rate $d(E_\gamma, x, y, z)$ was computed using

$$d(E_\gamma, x, y, z) = d_{1m}(E_\gamma) \left(\frac{1m}{distance} \right)^2 = \frac{d_{1m}(E_\gamma)}{(x^m - x)^2 + (y^m - y)^2 + (z^m - z)^2} \tag{4.2.9}$$

where $d_{1m}(E_\gamma)$ corresponds to the dose rate (Sv h^{-1}) at a distance of 1 m from a point source emitting 1 photon of energy E_γ (MeV) per second [54] (see Eq. 4.2.10).

$$d_{1m}(E_\gamma) = \begin{cases} 1.986 \times 10^{-17} & \text{for } E_\gamma < 0.053 \text{ MeV}, \\ 1.364 \times 10^{-13} & \text{for } 0.053 \text{ MeV} \leq E_\gamma < 1.12 \text{ MeV}, \\ 1.404 \times 10^{-13} & \text{for } E_\gamma \geq 1.12 \text{ MeV}. \end{cases} \tag{4.2.10}$$

The energies of the gamma emission lines and their probabilities p were taken from [55, 56].

A first validation of the outcome of Eq. 4.2.5 was done comparing its results with the tabulated values in the Swiss legislation (annex 3 column 6 of [50]) of the ambient dose equivalent rate at a distance of 1 m from a point source of 1 GBq. For instance, for a source of ^{60}Co the dose rate computed was equal to 0.332 mSv h^{-1} GBq^{-1}, ~10% below the value given by ORaP (0.366 mSv h^{-1} GBq^{-1}). Moreover, the dose rate of the pipe pieces, computed with this second approach, were also validated through comparison with FLUKA simulations, as shown in chapter 5.

After having measured the dose rate for each pipe piece (d_p^m) and computed the same quantity (d_p^{jer}) through Eq. 4.2.5, using the specific activity of each radionuclide from the JEREMY code for a unit beam loss, the ratio between both values could be used to scale the loss rate and, thereby, to normalize the IRAS of each piece, as shown in Eq. 4.2.11

$$IRAS_p^{Total} = \frac{d_p^m}{d_p^{jer}} \sum_i \frac{a_{jer}^i}{10^{cl_i}} = \frac{d_p^m}{d_p^{jer}} IRAS_{jer}^{Total}. \tag{4.2.11}$$

Hence, the total $IRAS_{colis}$ could be calculated by weighting by the mass of each piece using Eq. 4.2.12

$$IRAS_{colis}^{Total} = \frac{\sum_p M_p \; IRAS_p^{Total}}{M_{cont} + \sum_p M_p} = \frac{\sum_p M_p \; IRAS_p^{Total}}{M_{colis}}. \tag{4.2.12}$$

In the same way, the $IRAS_{lot}$ could be computed using Eq. 4.2.13

$$IRAS_{lot} = \frac{\sum_{colis} M_{colis} \; IRAS_{colis}^{Total}}{\sum_{colis} M_{colis}}. \tag{4.2.13}$$

As stated for the previous approach, the results of this second method will be discussed in the chapter 6.

CHAPTER 5

Computer Codes for Induced Activation

5.1 JEREMY

As previously mentioned, the JEREMY code[1] was used to compute the nuclide inventory, i.e. the list of radionuclides and their respective specific activities, present in the PS pipes after having being exposed during more than 40 years to ionizing radiations inside the PS tunnel.

A set of inputs are needed in order to compute the induced specific activities with the JEREMY code. As a first step, shown in Fig. 5.1, the particle spectra of the radiation field (fluence spectra) are calculated via Monte Carlo simulation. As shown later on, FLUKA was the code used to calculate the fluence spectra used in the characterization of the PS pipes. In a second step, the JEREMY code computes two different outputs:

- the isotope production rates from the fluence spectra, the isotope production cross sections and the chemical composition of the material;
- the induced specific activities of the produced radionuclides by using the irradiation history together with the isotopes decay data (see Fig. 5.1).

As mentioned in the previous chapter, both isotope production rates and induced specific activities from JEREMY are given for a loss rate of one primary beam particle per second. The loss rate is afterwards normalized either by scaling directly the beam loss rate if its value is known, or using a γ-spectrometry measurement of one radionuclide (finger-print procedure) or also through indirect normalization procedures, as the

[1] Code mainly implemented in PYTHON with some routines coded in ANSI C to reduce computation time. [23]

ones described in the previous chapter (specific activity vs. count rate and dose rate computation methods).

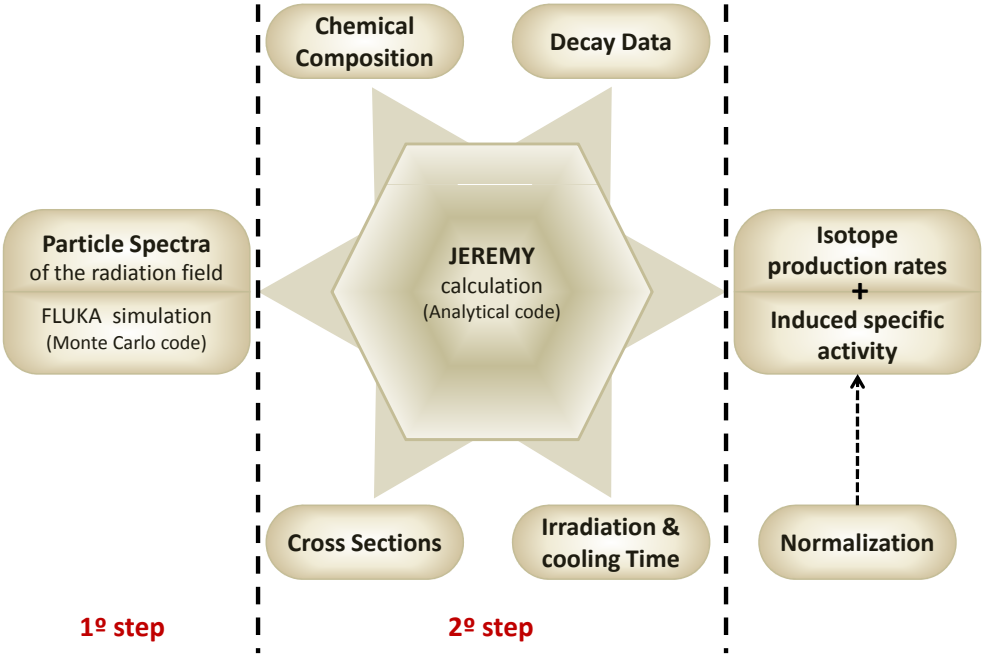

Figure 5.1: JEREMY code dataflow.

5.1.1 Mathematical Formulation

As described in detail in [23], the specific activity of nuclide b due to a beam loss rate of one primary particle per second is given in matrix form by Eq. 5.1.1

$$A_b = \sum_r \sum_e T_{br}\, P_{re}\, w_e. \tag{5.1.1}$$

The matrix P_{re} (see Eq. 5.1.2) describes the production rate ($P_{re} w_e$) of nuclide r from element e present in the material, while the matrix T_{br} (see Eq. 5.1.3) introduces the time evolution of the specific activity of nuclide b including the build-up of nuclide r and the full decay chain until nuclide b through the use of the Bateman coefficients (see Eq. 5.1.4). The index r represents all the nuclides directly produced from the target elements e of the material (w_e being the weight fraction of element e in the material (i.e. the fraction of the mass of element e (m_e) to the total mass of material (m_{mat})).

The matrices P_{re} and T_{br} are given by Eq. 5.1.2 and Eq. 5.1.3, respectively.

$$P_{re} = \frac{N_A}{M_e} \sum_{i=n,\gamma,p,\pi^+,\pi^-} \int \Phi_i(E)\, \sigma_{i,e,r}(E)\, dE, \tag{5.1.2}$$

$$T_{br}(t_{irr}, t_{cool}) = \sum_{c,r\to b} \sum_{m=1}^{j_c} \frac{c_m^c}{\lambda_m^c} e^{-\lambda_m^c t_{cool}} (1 - e^{-\lambda_m^c t_{irr}}), \tag{5.1.3}$$

with,

- $\sigma_{i,e,r}(E)$ [cm^2], the production cross section of nuclide r from element e by the particle i with kinetic energy E (weighted by the natural isotope abundances of each element e);
- $\Phi_i(E)$ [cm^{-2} s^{-1} eV^{-1}], the fluence of the particle i with kinetic energy E generated by one primary particle per second;
- N_A [mol^{-1}], the Avogadro constant, and M_e [g mol^{-1}], the molar mass of element e. The number of atoms of element e per gram of material is then given by $w_e \times N_A / M_e$;
- λ_m^c [s^{-1}], the total decay constant of the mth nuclide in the decay chain c (c running over all decay chains starting from nuclide r leading to nuclide b, with j_c the number of nuclides in a given decay chain c). For a decay chain containing branching decays, $\lambda_m^{c^*}$ denotes the partial decay constant of the mth nuclide in the decay chain c;
- t_{irr} [s] and t_{cool} [s], the irradiation and cooling times, respectively;
- c_m^c, the Bateman coefficients ($\lambda_i^{c^*}$ being the partial decay constant for the transformation of the ith to the $(i+1)^{th}$ nuclide in a decay chain c with branching decays):

$$c_m^c = \frac{\prod_{i=1}^{j_c} \lambda_i^{c^*}}{\prod_{\substack{i=1 \\ i\neq m}}^{j_c} (\lambda_i^c - \lambda_m^c)} = \frac{\lambda_1^{c^*} \lambda_2^{c^*} \lambda_3^{c^*} \cdots \lambda_{j_c}^{c^*}}{(\lambda_1^c - \lambda_m^c)(\lambda_2^c - \lambda_m^c) \cdots (\lambda_{j_c}^c - \lambda_m^c)}. \tag{5.1.4}$$

The validation of the JEREMY code was performed with different experiments at CERN. [57]

5.1.2 JEREMY Inputs

Fluence spectra

In 2011, shielding studies of the PS tunnel were performed near the injection region from the PSB (SS42 (see Fig. 3.8)) to evaluate the stray radiation profile at ground level

(route Goward) [58]. Since the neutrons dominate at surface level, their fluence spectra were computed by FLUKA simulation as a function of height from the PS tunnel until few meters above ground level and for two different proton beam momenta: 1.4 GeV c^{-1} and 14 GeV c^{-1}, corresponding to the beam momenta at injection from the PSB and at extraction to the SPS, respectively.

As previously mentioned (see Sec. 3.5), the radiation field of secondary particles expected at the distance of the PS chilled water pipeline to the beam line consists mostly of neutrons. Hence the neutron spectra from the aforementioned shielding studies were used for the characterization of the PS pipes (see Fig. 5.2). The outcome from JEREMY was then compared (see Sec. 5.1.3) using another set of spectra (from the SPS radiation environment) that includes the fluence of neutrons but also of protons and pions (already presented in Fig. 2.1).

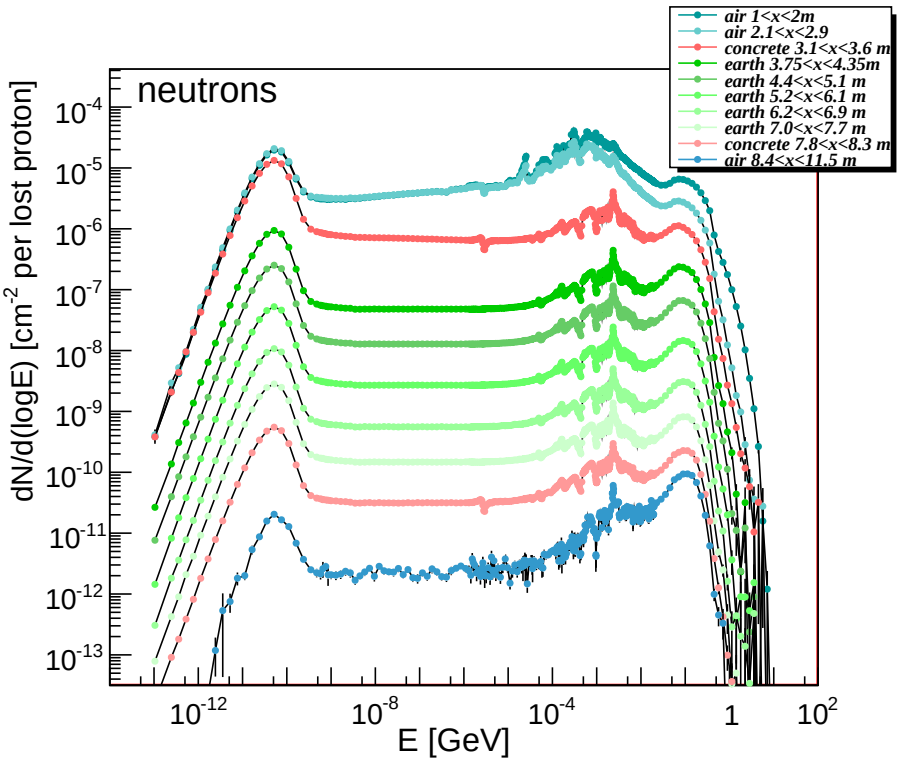

Figure 5.2: Neutron fluence spectra with a proton beam momentum of 14 GeV c^{-1}, calculated for different heights from the PS tunnel until the ground level [58]. The neutron spectrum used for the characterization of the PS pipes (located on the top of the tunnel) was the one corresponding, in this graph, to the height between 2.1 and 2.9 m.

Chemical composition

The chemical composition of the PS pipes was obtained using a mobile optical

Element	Mass percentage (average)
Fe	98.800
Mn	0.4553
C	0.2340
Si	0.1201
Al	0.1164
Cu	0.0770
W	0.0758
Ni	0.0346
Cr	0.0190
Pb	0.0152
Co	0.0051
Mo	0.0050
Zr	0.0050

Table 5.1: Chemical composition of the PS pipes (PMI-Master pro).

emission spectroscopy (OES) analyser, the PMI-Master pro (see Fig. 5.3), which relies on atom excitations from a high energy spark under argon atmosphere that vaporises part of the sample's surface. The resulting electron de-excitations can afterwards be converted into a spectral pattern which allows the analysis of the material composition.

Figure 5.3: Optical Emission Spectroscopy analyser (PMI-Master pro).

Tab. 5.1 presents the chemical composition of the PS pipes obtained with the PMI-Master pro, averaged over several measurement points.

To assess the PMI-Master pro reliability, the spectrometer was used with samples of different materials previously analysed by external laboratories. The results of the analysis of a stainless steel sample are presented in Tab. 5.2. One can see that there is an overall consistency between both analyses, also observed with samples of different ma-

Element	EIG (%)	PMI (%)
Fe	69.2	72.0
Cr	18.6	17.6
Ni	8.32	7.64
C	-	0.0659
Si	0.648	0.368
Mn	1.52	1.43
P	0.0302	*
S	0.037	*
Mo	0.567	0.236
Cu	0.393	0.352
Al	0.277	0.0032
Co	0.172	0.103
V	0.0704	0.0592
W	0.0407	< 0.03

* Not detectable with the PMI.

Table 5.2: Chemical composition analysis of a stainless steel sample (INOX RNDS 304L) from a external laboratory (Ecole d'Ingénieurs de Genève (EIG)) using the X-ray fluorescence spectrometry (XRF) technique and from the in situ mobile analyser (PMI-Master pro) using the OES technique.

terials not shown here. Despite some significant discrepancies, such as the aluminium in the stainless steel sample, a good level of confidence may be attributed the the PMI outcome.

Time evolution

As previously mentioned, the PS accelerator has the longest run period among all the CERN accelerators. With the first protons accelerated in 1959 and the last dismantlement campaign of the chilled water pipes in 2004, the upper limit of the irradiation time was, consequently, set at 45 years. Then, 7 years of cooling time have passed until the beginning of the radiological characterization. An analysis of the JEREMY results, with different irradiation and cooling times, is presented in the next section.

Cross sections and decay data

As described in [23], the isotope production cross sections for neutrons below 20 MeV were extracted from the JEFF 3.1.1 library [59] and for neutrons above 20 MeV, as well as for protons and pions were calculated using the code FLUKA. The isotopes decay data was also extracted from the JEFF 3.1.1 library.

Specific activity [Bq g^{-1}] (t_{irr} = 45 y + t_{cool} = 7 y)							
14 GeV (2.1 - 2.9 m)		**1.4 GeV (1.7 - 2.7 m)**		**450 GeV (0.5 - 1.0 m)**		**450 GeV (0.5 - 1.0 m)**	
n (PS)		**n (PS)**		**n (SPS)**		**n + p + π^+ + π^- (SPS)**	
Fe-55	1.16×10^{-08}	Fe-55	1.54×10^{-09}	Fe-55	6.91×10^{-07}	Fe-55	6.98×10^{-07}
H-3	6.25×10^{-10}	Co-60	5.38×10^{-11}	H-3	3.79×10^{-08}	H-3	4.86×10^{-08}
Co-60	3.17×10^{-10}	H-3	2.74×10^{-11}	Co-60	2.29×10^{-08}	Co-60	2.29×10^{-08}
Mn-54	3.13×10^{-11}	Ni-63	3.03×10^{-12}	Ni-63	1.27×10^{-09}	Mn-54	1.27×10^{-09}
Ni-63	1.88×10^{-11}	Mn-54	1.34×10^{-12}	Mn-54	1.20×10^{-09}	Ni-63	1.27×10^{-09}
Sc-44	5.59×10^{-12}	Sc-44	2.97×10^{-13}	Sc-44	3.93×10^{-10}	Sc-44	6.73×10^{-10}
Ti-44	5.59×10^{-12}	Ti-44	2.97×10^{-13}	Ti-44	3.93×10^{-10}	Ti-44	6.73×10^{-10}
V-49	4.97×10^{-12}	V-49	2.03×10^{-13}	V-49	2.86×10^{-10}	V-49	3.49×10^{-10}
Ar-39	1.18×10^{-12}	Ar-39	7.32×10^{-14}	Ar-39	9.25×10^{-11}	Ar-39	1.82×10^{-10}
Nb-93M	8.62×10^{-13}	Nb-93M	5.89×10^{-14}	Na-22	3.88×10^{-11}	Na-22	7.07×10^{-11}
Na-22	5.63×10^{-13}	Na-22	2.95×10^{-14}	Nb-93M	3.87×10^{-11}	Nb-93M	3.87×10^{-11}
Ni-59	1.61×10^{-13}	Ni-59	2.73×10^{-14}	Ni-59	1.14×10^{-11}	P-32	1.87×10^{-11}
...	...	...	...	...	...	...	...
	$\mathbf{1.26\times10^{-08}}$		1.62×10^{-09}		7.55×10^{-07}		7.74×10^{-07}

Table 5.3: Specific activities [Bq g^{-1}] by unit loss rate of the dominant radionuclides obtained from JEREMY with four different particle spectra and for irradiation and cooling times set at 45 and 7 years, respectively.

5.1.3 JEREMY Results

Tab. 5.3 presents part of the nuclide inventory[2] and the respective specific activities (for a loss rate of one primary proton per second) obtained from JEREMY, for four different radiation environments: two sets of particle spectra from the PS, at a distance from the beam line corresponding to the PS pipes location in the tunnel and for beam momenta of 1.4 GeV c^{-1} and 14 GeV c^{-1}; two from the SPS, both closer to the beam line (from ~0.5 to 1 m), for a proton beam momentum of 450 GeV c^{-1}, the first one for neutrons only and the second set of spectra including also protons and pions.

As seen in Tab. 5.3, the particle spectra influences strongly the induced activity computed by JEREMY. Nevertheless, the specific activity induced from protons and pions, in the case of the SPS spectra, can be considered as negligible if compared with the neutrons contribution, meaning that no significant error should be made when considering only neutrons for the characterization of the PS pipes. Moreover, for a lower beam energy and at a higher distance to the beam line, as happens with the PS pipes, the contribution of other particles than neutrons is expected to be even lower that in the SPS case. Finally, for the characterization of the PS pipes, the neutron spectrum from the 14 GeV c^{-1} PS proton beam momentum was chosen in detriment of the corresponding to the 1.4 GeV c^{-1} momentum, since it results in a higher proportion of ^{55}Fe relatively to

[2]The complete nuclide inventory includes around 90 radionuclides.

	t_{cool}				
t_{irr}	5	6	7	8	9
15	1.97×10^{-08}	1.54×10^{-08}	1.20×10^{-08}	9.41×10^{-09}	7.38×10^{-09}
25	2.03×10^{-08}	1.59×10^{-08}	1.24×10^{-08}	9.74×10^{-09}	7.67×10^{-09}
35	2.05×10^{-08}	1.60×10^{-08}	1.25×10^{-08}	9.84×10^{-09}	7.76×10^{-09}
45	2.05×10^{-08}	1.60×10^{-08}	$\mathbf{1.26\times10^{-08}}$	9.89×10^{-09}	7.80×10^{-09}
55	2.05×10^{-08}	1.61×10^{-08}	1.26×10^{-08}	9.92×10^{-09}	7.83×10^{-09}

Table 5.4: Total specific activities [Bq g^{-1}] by unit loss rate obtained with JEREMY for the neutron spectrum of 14 GeV c^{-1} beam momentum and for different irradiation and cooling times (in years).

^{60}Co, hence being a conservative approach when computing the IRAS factor.

Tab. 5.4 shows the sum of the specific activities of the nuclides obtained from JEREMY for different irradiation histories. One can see that after few decades of activity build-up the total specific activity is already close to saturation, meaning that the exact irradiation time is not a critical input for the PS pipes. Nevertheless, 45 years is the maximum possible irradiation time to which the pipeline could be exposed, resulting in the highest activity. On the other hand, setting the cooling time to 7 years is also a conservative approach since only a section of the pipeline was effectively removed from the PS tunnel in 2004, whereas the removal works of the others pipeline sections started ~10 years ago (see Sec. 3.5). Then, for a lower cooling time, the inferred ^{55}Fe contribution for the IRAS factor will be higher since its half life is lower than the one of ^{60}Co, nuclide to whose specific activity the normalization is done.

5.1.4 IRAS$_{\text{JEREMY}}$

After having chosen the neutron spectrum for a 14 GeV c^{-1} proton beam momentum and a time evolution corresponding to an activity build-up of 45 years followed by 7 years of decay, the IRAS factor could be computed using Eq. 3.7.1 applied to the nuclide inventory obtained from the JEREMY code (see Tab. 5.3). With the nuclide inventory given for a primary beam loss rate of one proton per second, the total IRAS factor from JEREMY ($IRAS_{jer}^{Total}$) comes also scaled to this beam loss and must be normalized as referred in the previous chapter and carried out in the next one. Therefore, the value of the IRAS factor for the radionuclide ^{60}Co was computed using its specific activity from the JEREMY output (see Tab. 5.3), as shown in Eq. 5.1.5

$$IRAS_{jer}^{Co60} = \frac{a_{jer}^{Co60}}{10^{cl_{Co60}}} = 3.172 \times 10^{-11}. \tag{5.1.5}$$

The total IRAS factor obtained by including the specific activities of the set of radionuclides present in the JEREMY nuclide inventory is given by Eq. 5.1.6

$$IRAS_{jer}^{Total} = \frac{\sum_i a_{jer}^i}{10^{cl_i}} = 4.767 \times 10^{-11}, \tag{5.1.6}$$

and the ratio between total and ^{60}Co IRAS factors, by Eq. 5.1.7

$$\frac{IRAS_{jer}^{Total}}{IRAS_{jer}^{Co60}} = 1.503. \tag{5.1.7}$$

5.2 FLUKA

The FLUKA Monte Carlo code calculates particle transport and interactions with matter, i.e. based on modern physical models[3] and for a large energy range[4], the code can simulate the interactions and evolution of all components of particle showers in matter. The reliance on particle simulations is nowadays widespread in different fields due to several factors as the availability of ever-increasing CPU power over the years and the need of accurate estimations frequently constrained by increasingly demanding radiological limits or by financial issues, while, on the other hand, the machine complexity grows continuously, as happened with the LHC. In this way, the FLUKA applications have increased over the years from radiation shielding to activation, dosimetry, detector design, radiotherapy (including hadrons and ions), etc [60].

5.2.1 FLUKA Inputs

As mentioned before, FLUKA was used in the course of this work to compare Monte Carlo simulations with the analytical dose rate computation of the pipe pieces used under the second process of normalization (see Sec. 4.2.2).

Without going into specifics[5], each line (called also "card") of the FLUKA input file (text file with extension .inp) corresponds to a specific command that must be provided for FLUKA scoring. At least the following cards have to be inserted: the information

[3] Including the generalized INC model mentioned in Sec. 2.3.

[4] About 60 different types of particles can be simulated with FLUKA, as: photons and electrons from 1keV to thousands of TeV, hadrons up to 20 TeV and neutrons down to thermal energies (as an exception, a cross section library of 260 neutron energy groups is used by FLUKA to simulate interactions of low energy neutrons (E < 20 MeV) with matter instead of modeling them by Monte Carlo simulations) [60].

[5] Further details can be found in [60]

on the radiation source, the geometry layout (which can also be kept in a separate file), the definition of the materials used, assigning them to the regions previously defined in the geometry description, and also the output (or "detector") requested.

In order to score the distribution of the dose equivalent rate around a pipe piece with FLUKA and thereafter compare the outcome with the analytical computation, the following inputs were set in the input file:

- In the card BEAM, which defines several beam characteristics, the command ISOTOPE was chosen in order to define the beam particle as being radioactive isotope decays: ^{60}Co for the case of the pipe pieces (specified in the card HI-PROPE). In the card BEAMPOS, the command CART-VOL was used to extend the source (^{60}Co) over the whole pipe piece;
- The geometry of the pipe piece was simplified to a rectangular parallelepiped (RPP) of 85 cm x 25 cm x 1 cm, corresponding approximately to the averaged dimensions of the pieces after having being compacted. The layer of air inside the compacted pieces was not take into account. The geometry implemented for this simulation was already shown in Fig. 4.7;
- The material selected was iron, afterwards assigned to the previously defined RPP;
- The card EMF was used to activate the transport of the electromagnetic particles emitted during the radioactive decays;
- The card RADDECAY was also used to take into account the radioactive decays, using the semi-analogue mode, i.e. with no request for cooling times and therefore with results expressed per unit primary weight;
- A binning detector was selected to score the dose equivalent distribution (DOSE-EQ), expressed in pSv per unit primary weight, for a (Cartesian) spatial region that extends to 1 m around the pipe piece.

The number of primary histories simulated was set at 10^8 radioactive isotope decays.

5.2.2 FLUKA Results

In accordance to the input described in the previous subsection, the outcome from FLUKA is shown in 3 different plots.

The distribution of the equivalent dose rate around the pipe piece, expressed in μSv h^{-1} per Bq g^{-1}, is shown for both superior and lateral views in Fig. 5.4 and 5.5, respectively.

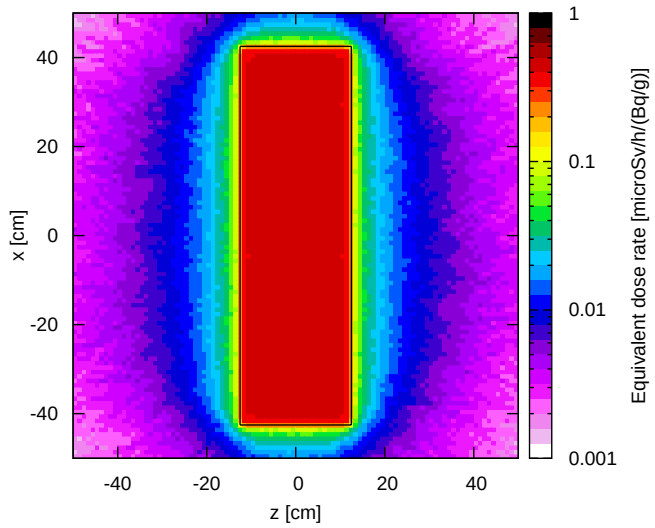

Figure 5.4: Equivalent dose rate (top view).

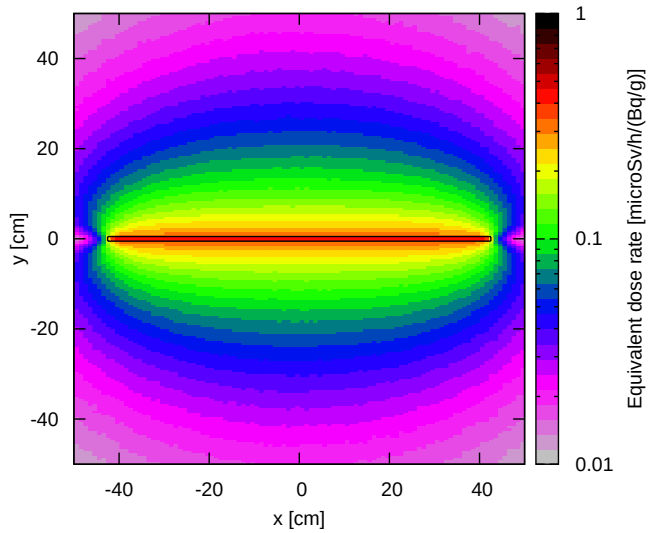

Figure 5.5: Equivalent dose rate (lateral view).

Fig. 5.6 shows the equivalent dose rate obtained for a 0.5 cm layer directly above the whole pipe piece. In accordance with this figure, one should not expect major variations of the equivalent dose rate for measurements performed at contact and slightly away from the center of the piece.

The outcome of the FLUKA simulation could then be compared to the values computed with Eq. 4.2.5, using the same inputs of density, geometry, etc. Fig. 5.7 shows both results and the ratio between them. One can see that, for a distance up to 1 m

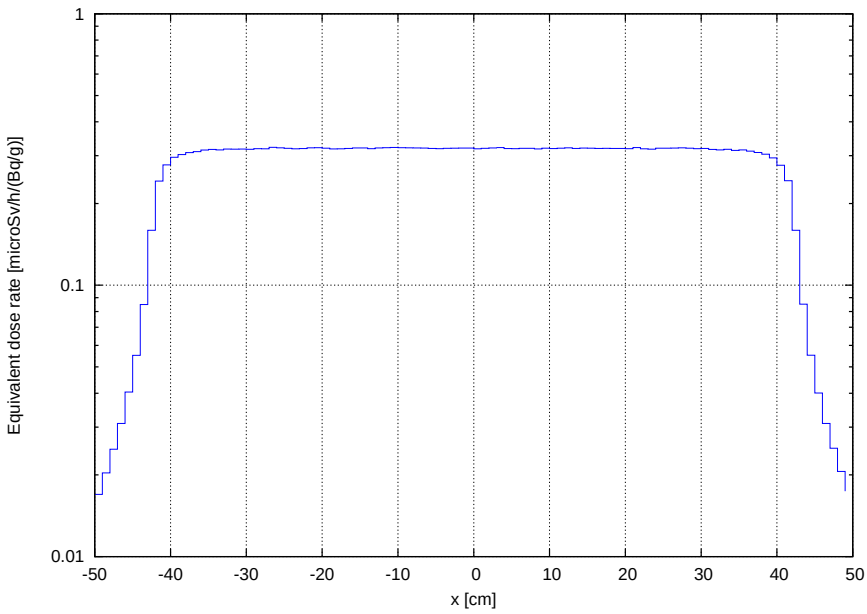

Figure 5.6: Equivalent dose rate for a layer of 0.5 cm directly above the pipe piece.

from the pipe piece, the ratio of values obtained by analytical computation and Monte Carlo simulation are always between 1 to 1.3, giving a good level of confidence to the analytical computation method and to the respective normalization approach of the IRAS factor.

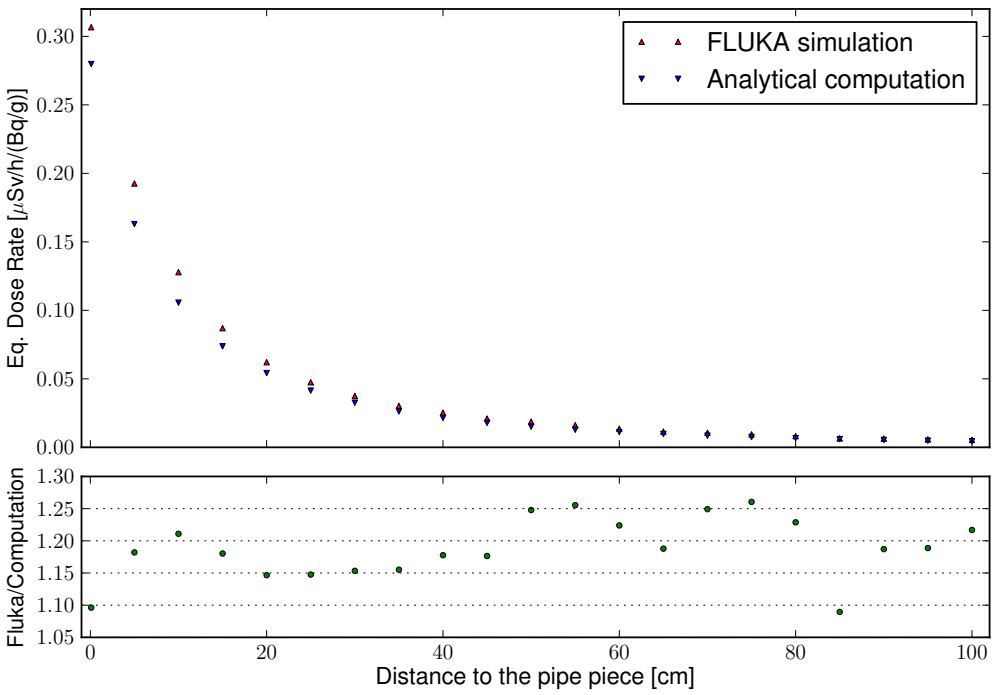

Figure 5.7: Simulation and analytical computation of the equivalent dose rate and ratio between both values, for a distance up to 1 m to the pipe piece.

A source for the observed slightly higher values from FLUKA lies in the fact that the code also transports photons scattered by the Compton effect while the linear attenuation coefficient (μ) used in Eq. 4.2.5 gives the total gamma ray attenuation in a narrow beam geometry with the scattered particles counted as lost [8].

Computations and simulations were further performed for different pipe piece lengths and widths, with the results as good as those shown in Fig. 5.7, confirming the reliability of the analytical method.

CHAPTER 6

Analysis of the Results

6.1 Spectrometry

Analysing the outcome from JEREMY for the chosen 14 GeV c^{-1} beam momentum (see Tab. 5.3), one can see that the X-rays emitter ^{55}Fe[1] appears as being the dominant radionuclide, followed by the low-energy beta emitter ^{3}H[2] with a specific activity close to the first expected gamma emitter ^{60}Co[3]. Nevertheless, despite having a lower specific activity than ^{55}Fe and ^{3}H, ^{60}Co provides the major contribution to the IRAS factor due to its lower TFA class (see Tab. 3.4).

In order to assess the reliability on the JEREMY nuclide inventory, samples were sent to the CERN gamma spectrometry service and to HEPIA for ^{55}Fe measurement[4]. The gamma spectrometry results pointed clearly to the presence of ^{60}Co with a specific activity close to the expected from the analysis performed in Sec. 3.5. Moreover, the presence of ^{55}Fe was also identified in both samples sent to HEPIA. Ratios of both ^{60}Co and ^{55}Fe specific activities, measured and predicted (see Tab. 5.3), are shown in Tab. 6.1.

[1] Mainly produced by low energy neutrons through the reaction $^{54}Fe(n, \gamma)^{55}Fe$ and decaying afterwards into ^{55}Mn by electron capture ($t_{1/2} \simeq 2.74$ y).

[2] Spallation product by high energy neutrons on the dominant element of the pipes material (iron, see Tab. 5.1). The tritium decays into ^{3}He by β^- decay ($t_{1/2} \simeq 12.32$ y).

[3] Produced mainly by low energy neutrons through the $^{59}Co(n, \gamma)^{60}Co$ reaction. ^{60}Co decays into ^{60}Ni by β^- decay ($t_{1/2} \simeq 5.27$ y) which, in turn, emits two gammas to reach its ground state.

[4] ^{55}Fe procedure: after dissolution of a few grams of sample by acid attack and other intermediate steps, a selective chromatographic resin (Eichrom TRU Resin) is used for iron separation. The specific activity of ^{55}Fe is then measured by liquid scintillation counting (LSC) (Packard 2900TR) and the separation yield determined by inductively coupled plasma mass spectrometry (ICP-MS 7500).

	Measurements			JEREMY
Sample	a^{Co60} [Bq g^{-1}]	a^{Fe55} [Bq g^{-1}]	a^{Fe55} / a^{Co60}	a^{Fe55} / a^{Co60}
RP_L_01b	0.442 ± 0.02	27 ± 8	61 ± 18	36 ± 2
RP_S_02b	2.54 ± 0.17	33 ± 8	13 ± 3	

Table 6.1: ^{60}Co and ^{55}Fe specific activities [Bq g^{-1}] (γ-spectrometry and HEPIA measurements) and ratio between both values, compared to the output from JEREMY.

The ratio between both ^{60}Co and ^{55}Fe specific activities could be roughly predicted using:

- tabulated thermal neutron capture cross-sections for the formation of both nuclides (^{54}Fe(n, γ)^{55}Fe and ^{59}Co(n, γ)^{60}Co): σ^{th}(^{54}Fe) = 2.3 b, σ^{th}(^{59}Co) = 37.2 b;
- saturation levels of both nuclides after 45 years of irradiation and 7 years of cooling time;
- iron and cobalt proportions in the pipes material (98.8% and 0.0051%, respectively (see Tab. 5.1)) jointly with natural isotopic compositions of ^{54}Fe (5.845%) and ^{59}Co (100%).

Fig. 6.1 depicts the time evolution of the activity of both radionuclides for a build-up of 45 years and decay of 7 years, normalized to their saturation activities. Taking only into account the (n, γ) cross-sections, one can see that the ratio between the ^{55}Fe and ^{60}Co specific activities should be around 30, close to the value predicted by JEREMY and also of the same order of magnitude as the measured ones.

Furthermore, the gamma spectrometry analysis had also revealed the presence of ^{44}Ti[5] with a much smaller specific activity than the one measured for ^{60}Co and with a higher associated error. In order to reduce the minimum detectable activity (MDA) and the measurement error of ^{44}Ti, the gamma spectrometry measurement was repeated extending the acquisition time from 2.8 hours, set for the previous measurements, to 15 hours. The results of the measurement are presented in Tab. 6.2 jointly with the ratios of measured and predicted ^{60}Co and ^{44}Ti specific activities.

In either of the presented cases, one may conclude that the outcome from JEREMY is in a good agreement with the performed measurements, since the deviations from both ratios using computed and measured specific activities are always below a factor

[5]Produced by spallation reaction with high energy neutrons mainly in iron. ^{44}Ti decays into ^{44}Sc by electron capture ($t_{1/2} \simeq 60.0$ y).

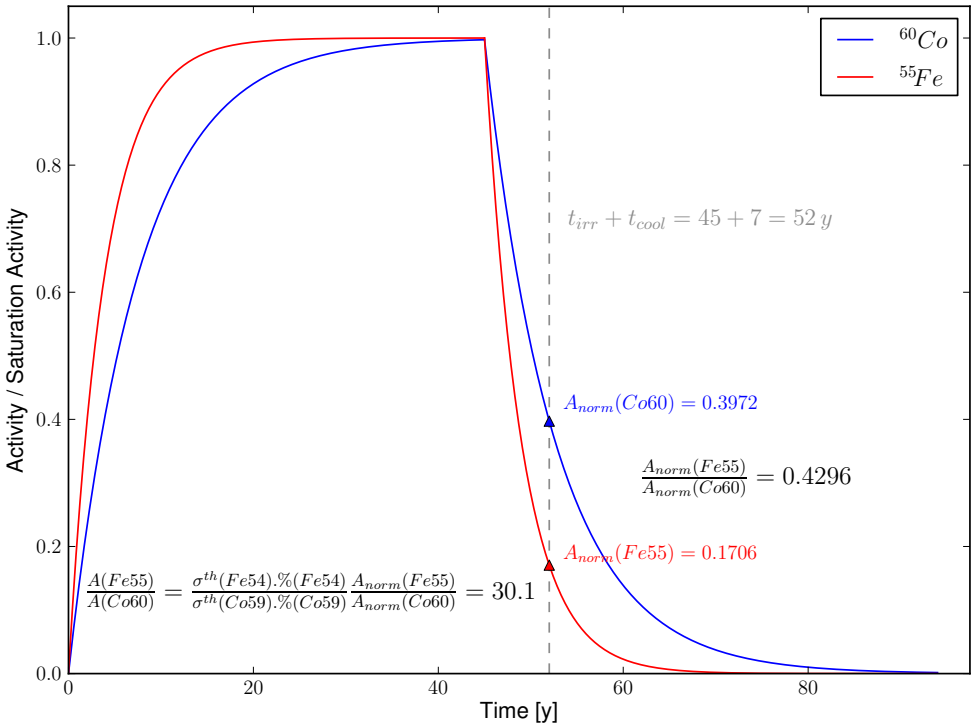

Figure 6.1: Activity build-up and decay of ^{60}Co and ^{55}Fe over time.

	Measurements			JEREMY
Sample	**a^{Co60} [Bq g^{-1}]**	**a^{Ti44} [Bq g^{-1}]**	**a^{Co60} / a^{Ti44}**	**a^{Co60} / a^{Ti44}**
RP_L_01c	0.484 ± 0.039	$6.8\times10^{-3} \pm 1.2\times10^{-3}$	71 ± 14	57 ± 4

Table 6.2: ^{60}Co and ^{44}Ti specific activities [Bq g^{-1}] measured by γ-spectrometry and ratio between both values, compared to the output from JEREMY.

of 3. For this reason, all the specific activities (and hence the proportions between them) used for the IRAS computation with Eq. 5.1.6 were the ones obtained from JEREMY.

6.2 Experimental Validation

In order to validate and compare both normalization processes described in the course of this work, 5.5% of the total length of the chilled water pipeline were characterized according to the strategy described in chapter 4. Fig. 6.2 presents the net count rate dispersion obtained with 84 pipe pieces measured with the FH 40G-L10 + FHZ 512 BGO external probe. From these measurements, it resulted a mean net count rate of 370.7 cps.

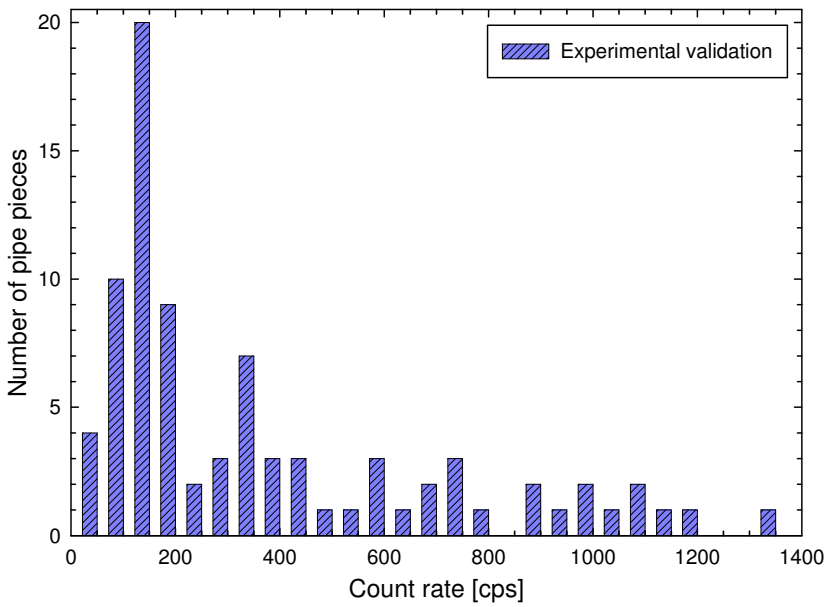

Figure 6.2: Histogram of the net count rate dispersion for a total of 84 measured pipe pieces.

The total $IRAS_{colis}$[6] of the 84 measured pipe pieces was computed according to the "specific activity vs. count rate" normalization method, using Eq. 4.2.3. It yielded a value of 0.533 (see Tab. 6.3), well below the maximum allowed $IRAS_{colis}$ of 10 for one primary package and of 1 for the $IRAS_{lot}$. Moreover, following the "dose rate ratio" normalization procedure, the total $IRAS_{colis}$, obtained using Eq. 4.2.12, was equal to 0.458 (see Tab. 6.3), close to the $IRAS_{colis}$ achieved with the previous method and hence yielding the same conclusion of radiological criteria fulfillness.

For the second method of normalization, the dose rate integration was performed for each pipe piece and using their true dimensions, previously measured in the course of the pre-conditioning process. The measurement point for the integral computation was set at a distance of 10 cm from the center of each piece. This distance was chosen since it was seen from previous analyses that it resulted in the best match between measured (SCINTO) and computed values[7].

Since the need of true dimensions and dose rate computations for each pipe piece

[6]For the IRAS computation, performed with both methods, the mass of the container was not added to the mass of the measured pieces as set by ANDRA and stated in Eq. 4.2.2. In fact this would have resulted in a lower $IRAS_{colis}$ but makes more sense to be done only for full containers.

[7]For this comparison, the specific activity and dose rate of several pieces were measured with the RADOS RTM661/440 and SCINTO, respectively. Then, the dose rate integral computation was performed using as input the measured specific activity (RTM) and the true dimensions of each piece, for a measurement point (x^m, y^m, z^m) set at several distances. Afterwards, the computed dose rates were compared with the SCINTO measurements, leading to the conclusion of best fit for a 10 cm distance.

	Normalization method		
	Specific activity vs. Count rate	**Dose rate ratio (true dimensions)**	**Dose rate ratio (standard dimensions)**
$IRAS_{colis}$	0.533	0.458	0.525

Table 6.3: $IRAS_{colis}$ of both methods of normalization: specific activity vs. count rate and dose rate ratio (with true and standard dimensions).

limit the operationality of the second method, standard pipe piece dimensions were established based on computation results and on the premise that the pipe piece dimensions are roughly the same, except for their width due to different pipe diameters. Assuming a 20 cm width average, the standard dimensions of 85 cm x 1 cm x 20 cm were established and used for the dose rate computation of the 84 pipe pieces. The total $IRAS_{colis}$ given by the second method of normalization, using standard piece dimensions, for a measurement point set at 10 cm of the center of the pipe piece, was equal to 0.525 (see Tab. 6.3). As it can be seen from the table analysis, also in this case the obtained $IRAS_{colis}$ is very close to the previous values meaning that the operationality of the second normalization method may be clearly envisaged. Moreover, the main error contributions for the $IRAS_{colis}$ shown in Tab. 6.3 might be attributed to measurement errors (count rate, dose rate, gamma spectrometry and chemical composition measurements) and to the uncertainty of the description of the radiation field by the neutron spectra.

Based on the fact that the experimental validation was performed with pipes selected at random, the $IRAS_{colis}$ obtained with both normalization methods shall be representative of the total batch of pipes. Nevertheless, the possibility cannot be ruled out that other parts of the pipeline have a much higher activation level, resulting in the non-compliance of the ANDRA's radiological acceptance criteria. However, this highly unlikely event can only be completely discarded after the characterization of the whole pipeline. On the other hand, the characterization of a larger percentage of the pipeline would have resulted in a higher confidence level on the criteria observance but due to operational reasons this has not been possible.

Finally, pipe pieces with non-standard shapes or with a hot spot shall be characterized in a slightly different way since problems might arise with the count rate or dose rate measurements and their correlation with the corresponding specific activity of the piece. In such cases, it is advised to measure the specific activity of the non-standard piece, for instance with the RADOS RTM661/440, and then use the obtained value directly in Eq. 4.2.2 to compute the $IRAS_{colis}$.

CHAPTER 7

Conclusions

Due to corrosion problems, the chilled water pipes, used for air-conditioning during more than 40 years, were removed from the PS tunnel during the long shutdowns between the years 2000 to 2004. The radiological characterization of the 1200 m of steel pipeline, exposed for several decades to ionizing radiation from the PS accelerator, started seven years after the last dismantlement campaign, in the second half of 2011.

The radiological characterization of the PS pipes described in the present study highlighted a nuclide inventory with ^{55}Fe as dominant radionuclide and ^{60}Co as dominant γ emitter. It was found that, together, they contributes to more than 90% of the computed IRAS factor of the PS pipes, with the measured ^{60}Co activity presenting the main contribution ($\sim$66.5%) and the inferred ^{55}Fe activity the remaining part. The calculated ratio of specific activities between both radionuclides was found to be in good agreement with the measurements, as shown in chapter 6.

Two different normalization methods of the IRAS factor were used in order to compare them and evaluate their operationality for future characterization processes. The first normalization method employs linear least squares fits between the specific activity and respective count rate measured from the radioactive materials being characterized. The second method is based on a ratio of dose rates: one being measured and the other computed analytically for each activated piece.

FLUKA and JEREMY computer codes had a key role for the work described in this thesis since the particle spectra of the radiation field around the PS pipes came from FLUKA Monte Carlo simulations and the radionuclide inventory from JEREMY analytical computations. FLUKA simulations were also performed in the course of this work for comparison with the analytical dose rate calculations, yielding very satisfactory results, as shown in chapter 5.

Of the total length of the pipeline, 5.5% were pre-conditioned and used for validation of the normalization methods described in this document. The $IRAS_{colis}$ obtained with both methods, specific activity vs. count rate and dose rate ratio, were equal to 0.533 and 0.458, respectively. Using standard pipe piece dimensions, the $IRAS_{colis}$ obtained with the dose rate ratio method was equal to 0.525.

The fulfilment of the ANDRA radiological acceptance criteria ($IRAS_{colis} < 10$ & $IRAS_{lot} < 1$) of the 70 m of the characterized pipeline, whichever method used, confirms the expected final elimination of the whole PS chilled water pipeline towards a TFA french repository.

References

[1] MARTIN J. *Physics for Radiation Protections*. Wiley-VCH, 2nd edition, 2006.

[2] Interactive chart of nuclides. Available at: `http://www.nndc.bnl.gov/chart/`. [Accessed 1 September 2012].

[3] MAGILL J., PFENNIG G., and GALY J. *Karlsruher Nuklidkarte*. European Commission, 7th edition, 2006.

[4] LEO W. *Techniques for Nuclear and Particle Physics Experiments*. Springer-Verlag, 2nd edition, 1994.

[5] SHULTIS J. and FAW R. *Fundamentals of Nuclear Science & Engineering*. Marcel Dekker, 2002.

[6] ALLDAY J. *Quarks, Leptons and the Big Bang*. IoP, 2nd edition, 2002.

[7] PYNN R. *Neutron scattering*. Los Alamos Science, 1990.

[8] BARBIER M. *Induced Radioactivity*. North-Holland Publishing Company, 1969.

[9] SULLIVAN A. *A Guide to Radiation and Radioactivity Levels Near High Energy Particle Accelerators*. Nuclear technology Publishing, 1992.

[10] CUGNON J., VOLANT C., and VUILLIER S. Nucleon and deuteron induced spallation reactions. *Nuclear Physics A*, 625:729–757, 1997.

[11] CUGNON J. A short introduction to spallation reactions. *Springer-Verlag*, 2011.

[12] LERAY S. Nuclear reactions at high energy. *CEA*, 2001.

[13] KNOLL G. *Radiation Detection and Measurement*. John Wiley & Sons, 3rd edition, 2000.

[14] Anon. *The Nuclear Physics and Reactor Theory Handbook*. U.S. Department of Energy, 1993.

[15] FERRARI A. and SALA P. The physics of high energy reactions. *INFN*, 1996.

[16] DAS A. and FERBEL T. *Introduction to Nuclear and Particle Physics*. World Scientific, 2nd edition, 2003.

[17] FOWLER M. Transforming energy into mass: Particle creation. *University of Virginia*, 2008.

[18] COTTINGHAM W. and GREENWOOD D. *Nuclear physics*. Cambridge University Press, 2nd edition, 2001.

[19] BASDEVANT J., RICH J., and SPIRO M. *Fundamentals in Nuclear Physics*. Springer, 2005.

[20] BERINGER J. et al. (Particle Data Group). Phys. Rev. *D86, 010001*, 2012.

[21] TOWNSEND J. *Quantum Physics*. University Science books, 2010.

[22] PODGORSAK E., editor. *Review of Radiation Oncology Physics*. IAEA, 2005.

[23] FROESCHL R., MAGISTRIS M., and THEIS C. Computation of radioactivity in particle accelerators and propagation of uncertainties with the JEREMY code. To be submitted to Nuclear Instruments and Methods in Physics Research, B.

[24] FROESCHL R., ULRICI L., and MICHAUD R. Computation of the nuclide inventory of ion exchange resins cartridges based on a dose rate measurement. *CERN*, 2011.

[25] SELZER S. et al. *Fundamental Quantities and Units for Ionizing Radiation. ICRU REPORT No. 85*. Oxford University Press, 2011.

[26] BRABY L. et al. *Quantification and Reporting of Low-Dose and other Heterogeneous Exposures. ICRU REPORT No. 86*. Oxford University Press, 2011.

[27] VALENTIN J., editor. *The 2007 Recommendations of the International Commission on Radiological Protection. ICRP PUBLICATION 103.* Elsevier, 2007.

[28] WERNLI C. External dosimetry: Operational quantities and their measurement. *11th International Congress of the International Radiation Protection Association (IRPA)*, 2004.

[29] SCHMIDT R. et al. Protection of the CERN Large Hadron Collider. *New Journal of Physics 8 290*, 2006.

[30] BRUNING O. et al., editors. *LHC Design Report. The LHC main ring*, volume I. CERN, 2004.

[31] ASSMANN R. et al. Studies on combined momentum and betatron cleaning in the LHC. *23rd Particle Accelerator Conference*, 2009.

[32] MAGISTRIS M. *Radiological Characterization of Radioactive Waste at CERN*. PhD thesis, Technischen Universitat Wien, 2008.

[33] EVANS L. The Large Hadron Collider. *Phil. Trans. R. Soc. A*, 370:831–858, 2012.

[34] PETERSEN K. et al. The protection system for the superconducting elements of the Large Hadron Collider at CERN. *Particle Accelerator Conference*, 1999.

[35] EVANS L. and BRYANT P., editors. *The Cern Large Hadron Collider: Accelerator and Experiments*. Institute of Physics Publishing and SISSA, 2008.

[36] BRACCO C. et al. Collimators and beam cleaning: First results and future plans. CERN, 2010.

[37] GILARDONI S. and MANGLUNKI D., editors. *Fifty years of the CERN Proton Synchrotron*, volume I. CERN, 2011.

[38] PLASS G. The CERN proton synchrotron: 50 years of reliable operation and continued development. *Eur. Phys. J. H*, 36:439–454, 2011.

[39] Proton Synchrotron - BE Department (CERN). Available at: `https://espace.cern.ch/be-dep/OP/PS/default.aspx`. [Accessed 1 September 2012].

[40] DAMJANOVIC S., ROESLER S., and WIDORSKI M. Shielding studies for the ground level above Straight Section 16 of the PS. *EDMS 1161800. CERN-DGS-2011-066-RP-TN*, 2011.

[41] DUMONT G. Radiation survey results 2011. PS complex. *EDMS 1179664. CERN*, 2012.

[42] The map of septa in the PS complex. Available at: `http://psdata.web.cern.ch/psdata/www/septa/pmap.htm`. [Accessed 1 September 2012].

[43] BRUNO L. et al. PS radiation working group. *EDMS 1142005. CERN-ATS-2011-007*, 2011.

[44] PRANTL F. and BAARLI J. *Control of Radioactive Pollution in the Environment of the CERN Accelerators*. CERN, 1972.

[45] LAMBERET C. et al. Démontage et traitement des tuyauteries d'eau glacée du tunnel PS. *EDMS 481193. CERN-SC-2004-049-RP-SN*, 2004.

[46] PRINCIPE R. and KUHNL-KINEL J. Year 2000 performance report. *CERN-ST-2000-052*, 2001.

[47] Safety policy at CERN (SAPOCO 42). Available at: `http://safety-commission.web.cern.ch/safety-commission/sapoco42/`. [Accessed 1 September 2012].

[48] Safety code F. CERN, 2006.

[49] ROESLER S. and THEIS C. Exemption and clearance of material at CERN. *EDMS 942170. CERN*, 2009.

[50] 814.501 Ordonnance sur la Radioprotection (ORaP) du 22 juin 1994 (Etat le 1 janvier 2012).

[51] ULRICI L. and BRUNO L. Radioactive waste. CERN communication, 2011.

[52] Les déchets provenant des installations INB. EDMS 328824. CERN.

[53] Décret n.2012-542 du 23 avril 2012. Journal Officiel de la République Française.

[54] ATCHISON F. Determination of the total nuclide inventory. *Scientific and Technical Report AN-99-01-14. PSI*, 1999.

[55] ECKERMAN K., WESTFALL R., RYMAN J., and CRISTY M. Nuclear decay data files of the dosimetry research group, 1993. Program NUCDECAY ORNL/TM-12350, RSICC Data Library Collection.

[56] CHU Y., EKSTROEM L., and FIRESTONE R. The Lund/LBNL Nuclear Data Search, 1999.

[57] FROESCHL R., MAGISTRIS M., and PEREIRA F. JEREMY - A code for radiological characterization of accelerator components including detailed uncertainty estimation. *ARIA2011, Second International Workshop on Accelerator Radiation Induced Activation, Ma'ale Hachamisha, Judean Hills (Israel), May 15-19*, 2011.

[58] DAMJANOVIC S., WIDORSKI M., and GILARDONI S. Shielding studies for the Route Goward / PS crossing. *EDMS 1161799. CERN-DGS-2011-065-RP-TN*, 2011.

[59] SANTAMARINA A. The JEFF-3.1.1 Nuclear Data Library. *Technical Report JEFF Report 22. Nuclear Energy Agency, Paris*, 2009.

[60] FERRARI A., SALA P., FASSÒ A., and RANFT J. *FLUKA: a multi-particle transport code*. CERN-2005-10, INFN TC-05/11, SLAC-R-773, 2011.

Acknowledgements

A stay at CERN in 2006 to visit the CMS and ATLAS experiments, that were in construction at that time, awakened my interest in working, one day, in this fantastic place. The opportunity arose in 2010 to develop the present project in the Radiation Protection Group. Thanks Robert for choosing me (!) and for all the moments spent discussing Physics.

I would also like to extend my thanks to João Carvalho, Luisa Ulrici, Nick Walter and last but surely not least to my family for all the support.